

Homologous and Mitochondrial Targeting Synergistic Induction of Apoptosis and Ferroptosis Enhanced PDT Performance Against Osteosarcoma HOS

Yang Wang

Chongqing Medical University

Liang Zhang

Chongqing Medical University

Guosheng Zhao

Chongqing Medical University

Yuan Zhang

Chongqing Medical University

Fangbiao Zhan

Chongqing Medical University

Zhiyu Chen

Chongqing Medical University

Tao He

Chongqing Medical University

Yang Cao

Chongqing Medical University

Lan Hao

Chongqing Medical University

Zhigang Wang

Chongqing Medical University

Zhengxue Quan

Chongqing Medical University

Yunsheng Ou (✉ ouyunsheng2001@163.com)

Chongqing Medical University

Research

Keywords: PDT, OS, Homologous targeting, Mitochondrial targeting, Ferroptosis

Posted Date: August 10th, 2021

DOI: <https://doi.org/10.21203/rs.3.rs-779156/v1>

License:  This work is licensed under a Creative Commons Attribution 4.0 International License.

[Read Full License](#)

Abstract

Background: There have been no prominent advancements in osteosarcoma (OS) treatment in the past 20 years. Although photodynamic therapy (PDT) is an emerging technique for cancer therapy, its lack of targeting in OS treatment severely limits its applications.

Methods: In this study, we constructed a potential theranostic nanoplatform by using (poly (ethylene glycol) polylactic-co-Glycolic acid (PEG-PLGA) nanoparticles (NPs) wrapping IR780 into the core (PEG-PLGA-IR780 NPs), which was further camouflaged with human OS cell membranes from the HOS cell line (MH-PEG-PLGA-IR780 NPs) to show homologous and mitochondrial targeting capacities. In addition, the potential underlying anticancer mechanisms of MH-PEG-PLGA-IR780 NPs-mediated PDT was investigated.

Results: We demonstrated that the MH-PEG-PLGA-IR780 NPs had excellent tumor/mitochondrial targeting with the help of homologous targeting to HOS cell line. Moreover, the excellent photoacoustic (PA)/fluorescence (FL) imaging ability of MH-PEG-PLGA-IR780 NPs laid a foundation for further applications. Under near-infrared (NIR) irradiation, we demonstrated that dual-targeting NPs-mediated PDT could significantly induce HOS cell apoptosis and ferroptosis, and further explored apoptosis was triggered by cytochrome c-activated mitochondrial apoptosis (endogenous apoptosis), and the specific molecular mechanisms of ferroptosis is the activation of NCOA4-mediated ferritinophagy and the passivation of GPX4 in vitro, synergistically leading to the excessive accumulation of ROS. In addition, MH-PEG-PLGA-IR780 NPs-induced PDT also showed an obvious inhibitory effect on tumor growth in vivo.

Conclusion: These results suggest the dual-targeting-based theranostic nanoplatform provides an effective method to improve PDT performance in OS and paves a new and promising way for OS therapy.

Background

Surgery and neoadjuvant chemotherapy are the main clinical treatments of osteosarcoma (OS), but the 5-year survival rate of patients with OS remains between 65%-70% [1]. As a potential anticancer therapeutic method, PDT induces cell death by depending on the accumulation of cytotoxic reactive oxygen species (ROS) [2, 3]. However, the use of photosensitizer alone has the disadvantages of fast metabolism and short blood circulation time in vivo. In particular, the poor targeting of PDT to OS seriously limits its clinical application [4]. In addition, due to tumor heterogeneity, activation of the epithelial-mesenchymal transformation (EMT), multidrug resistance and the complex microenvironment of tumors, PDT cannot effectively eradicate tumors by using a single mode of cell death [5]. Therefore, overcoming the poor targeting properties of PDT and inducing multiple modes of cell death to treat OS should be considered as advanced strategies to improve the innate characteristics of PDT.

Tumor cell and mitochondria targeting photosensitizer-based nanoplatforms were desirable to enhance PDT performance. IR780, a heptamethine cyanine molecule, has been used as a probe for the FL/PA imaging and of tumors in vivo. The lipophilic and cationic properties of IR780 could contribute to its

preferential intracellular accumulation in the mitochondria without the need for additional chemical conjugation with targeting ligands, which leads to the production of a large amount of ROS that damages the mitochondria under NIR irradiation (808 nm) [6-8]. Moreover, it has been reported that IR780 can penetrate deeper into tumor tissues [9]. Studies have also reported that NPs wrapped IR780 increased the PDT and photothermal therapy (PTT) performance by mitochondria dysfunction in other cancers [10-12]. Unfortunately, based on our prophase experimental results, the phagocytic and mitochondrial targeting effects of the PEG-PLGA-IR780 NPs were not satisfactory for OS cells, which may be related to tumor heterogeneity and the biocompatibility of the NPs (Figure S1).

With the rapid development of nanotechnology, utilizing cell membranes for nanoparticle surface functionalization presents a potential targeting method. In addition, cancer cell membranes have been demonstrated to endow NPs with the capability to target tumors by their homologous targeting properties and immune escape ability [13, 14]. This biomimetic engineering strategy of coating NPs with cell membranes could be successfully implemented due to its unique advantage of completely replicating the surface antigenic diversity of the source cells onto the engineered NPs. Therefore, based on this emerging method, PEG-PLGA-IR780 NPs were camouflaged with human OS cell membranes from the HOS cell line, aiming to synthesize dual-targeting (membrane-HOS-PEG-PLGA-IR780, MH-PEG-PLGA-IR780) NPs with homologous and mitochondrial targeting properties to improve the affinity of the NPs to OS and enhance PDT efficiency.

The main death mode of singlet oxygen-mediated PDT against solid tumors has long been considered as apoptosis [15-18]. However, the phenotypic diversity of tumor cells and activation of anti-apoptotic pathways may lead to tumor resistance to apoptosis, which promotes tumor relapse and metastasis [19-21]. As a new form of regulated cell death (RCD), ferroptosis is dependent on the overproduction of tailored lipid peroxides (LPOs), the excessive accumulation of the cellular labile iron pool (LIP) and defective lipid peroxidation repair by inhibiting glutathione peroxidase4 (GPX4) [22]. Recent studies have reported that targeting ferroptosis-associated tumor metabolism can eliminate resistant tumor cells [23, 24]. In addition, the excessive accumulation of redox-active ions is helpful to improve the performance of PDT by accumulating ROS through the Fenton reaction [25, 26]. Therefore, combining the induction of ferroptosis and apoptosis may be a highly promising therapeutic approach to potentiate the anticancer activity of PDT. In the present study, our results demonstrated that dual-targeting-based theranostic nanoplateform-mediated PDT exhibited a significant killing effect by the synergistic induction of apoptosis and ferroptosis in vitro and remarkably inhibited tumor growth, which were implemented by homologous and mitochondrial targeting. Moreover, the possible molecular pathway underlying this targeted PDT effectiveness was also discussed (Scheme 1).

Reagents And Methods

Reagents

Biocompatible PEG-PLGA (50:50, MW: 12,000 Da) was obtained from Ruixi Biotech Co., Ltd. (Xian, China). IR780 iodide, G418 and B27 were purchased from Sigma-Aldrich (St. Louis, MO, USA). Dichloromethane (CH_2Cl_2) was purchased from Beijing Bailingwei Technology Corp. (China). MitoTrackerTM Deep Red FM (MitoTracker) and C-11 BODIPYTM 581/591 (C11-BODIPY) were purchased from Thermo Fisher Corp (USA). Foetal bovine serum (FBS) and Dulbecco's-modified Eagle's medium (DMEM) were purchased from HyClone (Logan, UT, USA). The cell viability and cytotoxicity test kit, namely, Cell Counting Kit-8 (CCK-8), Liperfluo and FerroOrange were purchased from Dojindo Molecular Technologies (Kimamoto, Japan). The annexin V-FITC/propidium iodide (PI) double-staining test kit was purchased from KeyGen Biotech (Nanjing, China). RIPA lysis buffer, phenylmethanesulfonyl fluoride (PMSF), a bicinchoninic acid (BCA) protein assay kit, Membrane and Cytosol Protein Extraction Kit (cat. P0033), bovine serum albumin (BSA), 1,1'-dioctadecyl-3,3',3'-tetramethylindocarbocyanine perchlorate (Dil), a JC-1 mitochondrial membrane potential (MMP) assay kit (cat. C2006), a Membrane and Cytosol Protein Extraction Kit (cat. P0033), 2,7-dichlorodihydrofluorescein-diacetate (DCFH-DA) (S0033S), N-acetyl-L-cysteine (NAC) (cat. S0077), an adenosine triphosphate (ATP) assay kit (cat. S0026) and mouse anti-human GAPDH (cat. AG019-1) were obtained from Beyotime Biotech (Shanghai, China). YF633-Phalloidin was sourced from Evrbright, INC (US). Rabbit anti-human Bax (cat. D2E11), rabbit anti-human Bcl-2 (D55G8) (cat. 4223), rabbit anti-human cytochrome c (cat. 11940), rabbit anti-human cleaved caspase-7 (cat. 8438), rabbit anti-human cleaved caspase-9 (cat. 20750), rabbit anti-human cleaved caspase-3 (cat. 9664), and a ferroptosis Antibody Sampler Kit (cat. 29650) were purchased from Cell Signaling Technology (Boston, MA, USA). Z-VAD-FMK (cat. S7023), necrostatin-1 (Nec-1) (cat. S8037), bafilomycin A1 (Baf-A1) (cat. S1413), ferrostatin-1 (Fer-1) (cat. S7243) and deferoxamine (DFO) (cat. S5742) were sourced from Selleck (Houston, USA). PCNA (cat. 10205-2-AP) and Ki67 (cat. 27309-1-AP) were obtained from Proteintech (USA). Epidermal growth factor (EGF), basic fibroblast growth factor (bFGF) was obtained from PeproTech (USA).

Cell culture

The human OS cell lines HOS, MG63, and 143B, the murine OS cell line K7M2, murine breast cancer line 4T1 cells, and human non-small-cell lung cancer A549 cells were purchased from the American Type Culture Collection (ATCC, Manassas, VA, USA) and maintained in DMEM supplemented with 10% FBS, 100 $\mu\text{g}/\text{mL}$ penicillin and 100 $\mu\text{g}/\text{mL}$ streptomycin. Cells were maintained in a humidified atmosphere with 5% CO_2 at 37 °C. The human fetal osteoblastic cell line HFOB 1.19 was also obtained from the ATCC, and the cells were cultured in Dulbecco's modified Eagle's Medium F-12 nutrient mixture (DMEM/F12) supplemented with 2.5 mM of L-glutamine, 0.3 mg/mL of G418 in addition to 10% FBS, 100 $\mu\text{g}/\text{mL}$ penicillin and 100 $\mu\text{g}/\text{mL}$ streptomycin. HFOB 1.19 cells were maintained in a humidified 5% CO_2 atmosphere at a permissive temperature of 34 °C.

Synthesis of the MH-PEG-PLGA-IR780 NPs

i) The water-in-oil-in-water (W/O/W) double-emulsion method was used to synthesize PEG-PLGA-IR780 NPs. Briefly, PEG-PLGA (50 mg) and IR780 (2 mg) were dissolved in CH_2Cl_2 , and then the primary

emulsification was emulsified using an ultrasonic probe (Sonics & Materials, Inc., USA) (50 W, 3 minutes). Subsequently, 4% polyvinyl alcohol (PVA) (10 mL) was added to the emulsified solution, which was homogenized by a second sonication to form a W/O/W double emulsion (35 W, 3 minutes). Then, 2% isopropanol solution (10 mL) was added to the prepared emulsion which was mechanically stirred for 2 h to remove the CH₂Cl₂ followed by centrifugation (12,000 rpm for 6 minutes) to obtain the PEG-PLGA-IR780 NPs. ii) To prepare the HOS cell membranes, HOS cells were grown in T-75 culture flasks to full confluence and detached with 2 mM EDTA in phosphate-buffered saline (PBS), and washed three times in PBS by centrifuging at 800 rpm for 5 minutes. Subsequently, the cells were lysed with Membrane and Cytosol Protein Extraction Kit A containing PMSF (100:1), at -80°C with repeated freeze-thaw cycles followed by centrifugation (800 rpm for 5 minutes) to collect the cellular supernatant, finally, the precipitate after centrifugation at 12,000 rpm for 30 minutes, was the HOS cell membrane (MH). iii) MH-PEG-PLGA-IR780 NPs were finally synthesized by physically extruding the mixture of PEG-PLGA-IR780 NPs and the MH at the same concentration for 11 passes through a 400 nm polycarbonate porous membrane on a mini extruder (Avanti Polar Lipids, USA). The final product was stored at 4 °C for later use.

Characterization of the MH-PEG-PLGA-IR780 NPs

The size distribution, and zeta-potentials of various NPs and their stability of the NPs in fetal blood serum (10%) and PBS over seven days were determined using dynamic light scattering (DLS, Malvern Instruments, UK). The morphologies and structures of the NPs were observed using transmission electron microscopy (TEM, Hitachi H-7600, Japan). The optical absorption of the different NPs and free IR780 was determined with an ultraviolet-visible (UV-vis) spectrophotometer (US-2550, Shimadzu, Japan). A standard concentration curve of free IR780 measured at a wavelength of 798 nm was constructed to calculate the amount of IR780 encapsulated into the MH-PEG-PLGA NPs. The encapsulation efficiency (EE) and encapsulation content (EC) of IR780 were calculated by Equations (1) and (2)

$$(1) EE_{IR780} (\%) = (\text{mass of total IR780} - \text{mass of untrapped IR780}) / \text{mass of total IR780} \times 100\%$$

$$(2) EC_{IR780} (\%) = (\text{mass of total IR780} - \text{mass of untrapped IR780}) / \text{mass of total PEG-PLGA NPs} \times 100\%$$

Cellular uptake and deep penetration capability of the MH-PEG-PLGA-IR780 NPs

Laser confocal scanning microscopic (CLSM; Nikon A1+R, Japan) and Flow Cytometry (FC; BD FACSVantage SE, USA) were used to detect the cellular uptake of different NPs. Typically, HOS cells (1×10⁵/dish) were seeded into a laser confocal cell-culture dish. After 24 h of incubation, the culture medium was replaced with the serum-free medium containing PEG-PLGA NPs, PEG-PLGA-IR780 NPs or MH-PEG-PLGA-IR780 NPs (stained with Dil; λ excitation/λ emission = 549nm/565nm) for 1, 2, 3 or 4 h (IR780, 20 µg/mL). Then, the cells were fixed in 4% formaldehyde for 10 minutes and washed with PBS. After incubation for different time intervals with various NPs, the cell nuclei were stained blue with DAPI (λ excitation/λ emission = 364 nm/454 nm). The fluorescence images were directly recorded by CLSM.

Moreover, the quantitative cellular uptake of PEG-PLGA NPs, PEG-PLGA-IR780 NPs and MH-PEG-PLGA-IR780 NPs at different time intervals was quantified and analyzed by FC.

The penetration of the MH-PEG-PLGA-IR780 NPs was estimated in vitro using 3D tumor spheroid models. HOS tumor spheres (1×10^5 /well) were cultured in 6-well ultra-low attachment plates (Corning, Tewksbury, MA) in stem cell medium that consisted of serum-free DMEM/F12 with 20 ng/mL EGF, 20 ng/mL bFGF and B27. The medium was changed every two days over ten days. Then, the medium was replaced by the Dil-labelled NPs dispersed in DMEM/F12 (1 mL, 20 μ g/mL). After 4 h of coincubation, the 3D tumor spheroids were stained with DAPI for 10 minutes, and observed using CLSM.

Mitochondrial location and macrophage uptake assay

To verify the mitochondrial location of the MH-PEG-PLGA-IR780 NPs, MitoTracker was used to label mitochondria. Typically, HOS cells (1×10^5 /dish) were seeded into a laser confocal cell-culture dish for 24 h of incubation. Before the test, the growth medium was replaced with Dil labeled NPs (PEG-PLGA NPs, PEG-PLGA-IR780 NPs or MH-PEG-PLGA-IR780 NPs) at a concentration of 20 μ g/mL for a 4 h of coincubation. Then, the cells were fixed in 4% formaldehyde for 10 minutes and washed with PBS. Next, the HOS cell mitochondria were labelled with MitoTracker (λ excitation/ λ emission = 644 nm/665 nm) for 30 minutes, followed by 10 minutes of staining with DAPI. Finally, the mitochondrial localization of the NPs was observed using CLSM, and the Pearson correlation (PC) coefficients of each image were measured. This same staining method was used for 4T1, A549, MG63, 143B, K7M2 and HFOB 1.19 cells to identify the homologous targeting capabilities of the MH-PEG-PLGA-IR780 NPs.

Next, to verify the immune escape ability of the MH-PEG-PLGA-IR780 NPs, RAW 264.7 cells (1×10^5 /dish) were seeded in a laser confocal cell-culture dish. After a 24 h of incubation, the growth medium was replaced with serum-free medium containing Dil labeled NPs (20 μ g/mL) for 4 h of coincubation. Subsequently, the cells were fixed in 4% formaldehyde for 10 minutes and washed with PBS, YF633-Phalloidin and DAPI were used to label the cytoskeleton and nuclei of the RAW 264.7 cells within 10 minutes and 30 minutes, respectively. The uptake of various NPs by macrophages was finally observed by CLSM.

FL imaging/biodistribution and PA imaging of the MH-PEG-PLGA-IR780 NPs In vivo

HOS tumor-bearing mice were intravenously injected with MH-PEG-PLGA-IR780 NPs suspension (2 mg/mL, 200 μ L). Subsequently, NIR FL images were collected, pre-injection and at 1, 2, 3 and 6 h post-injection, and the relative FL intensity of each tumor region was measured by IndiGo 2.0.5.0 (Berthold Technologies, Germany). Ex vivo imaging was performed on the major organs and tumor tissues at 6 h post-injection to detect the biological distribution of the MH-PEG-PLGA-IR780 NPs.

A Vevo LAZR Photoacoustic Imaging System (VisualSonics Inc., Toronto, Canada) was used to determine the PA performance of the MH-PEG-PLGA-IR780 NPs. It has been reported that the PA signal intensity of IR780 is the greatest at the activation wavelength of 798 nm [27]. HOS tumor-bearing mice were

intravenously injected with a MH-PEG-PLGA-IR780 NPs suspension (2 mg/mL, 200 μ L). PA images were collected at different time points (pre-injection, 1, 2, 3 and 6 h post-injection), and the corresponding PA signal intensities were measured with a Vevo LAZR System.

Cell viability assay

A CCK-8 assay was used to determine cell viability after the different treatments. Briefly, HOS cells were seeded into 96-well plates at a density of 5,000 cells/well and incubated overnight for adherence. To determine the safety of the different NPs in vitro, HOS cells were incubated with various concentrations of NPs (NPs: 0.0, 0.2, 0.4, 0.6, 0.8, 1.0 mg/mL, and IR780: 0.0, 6.5, 13.0, 19.5, 26.0, 32.5 μ g/mL) for different length of time (0, 12, 24 and 48 h). To assess the change in cell viability after pretreatment with different inhibitors (z-VAD-FMK, Nec-1, Baf-A1, DFO, Fer-1, NAC), HOS cells were pre-incubated with the aforementioned inhibitors for 24 h before exposure to MH-PEG-PLGA-IR780 NPs-associated PDT. Following different treatments, 10 μ L of CCK-8 to added to each well followed by incubation for an additional 1 h. Finally, the plates with cells were placed in a microplate reader (MK3, Thermo Scientific) to measure the absorbance at 450 nm. Cell viability was calculated using the following formula: cell viability (%) = experimental group absorbance value/control group absorbance value \times 100%.

Measurement of intracellular ROS

Intracellular ROS was detected using DCFH-DA (λ excitation/ λ emission = 488 nm/530 nm). Typically, HOS cells (1×10^5 /dish) were seeded into a laser confocal cell- culture dish. After a 24 h of incubation, the medium was replaced by serum-free medium with or without NPs (PEG-PLGA-IR780 NPs or MH-PEG-PLGA-IR780 NPs (IR780: 20 μ g/mL)) followed by incubation for another 4 h. Then, the cells in the laser group received irradiation with an 808 nm laser at a power density of 1.5 W/cm² for 2 minutes. Then, the cells were incubated in serum-free medium containing 10 μ M DCFH-DA in the dark at 37°C for 30 minutes. Next, the cells were washed with PBS to remove excess DCFH-DA. Finally, the cells were immediately observed by CLSM to detect the intracellular ROS levels, treated with trypsin, collected in 200 μ L PBS and detected by FC.

MMP assay

The MMP ($\Delta\psi_m$) was detected using a JC-1 assay kit. HOS cells (1×10^5 /dish) were seeded into a laser confocal cell- culture dish for a 24 h of incubation. After adherence, the HOS cells were divided into different treatment groups (control, laser alone, PEG-PLGA-IR780 NPs, laser+PEG-PLGA-IR780 NPs, MH-PEG-PLGA-IR780 NPs, and laser+MH-PEG-PLGA-IR780 NPs (IR780: 20 μ g/mL)). After 4 h of intervention, all cells were cultured in fresh medium containing 1 mL of JC-1 staining solution (10 μ M) and incubated for 30 minutes in the dark at 37 °C under 5% CO₂. Then, the cells were washed with ice-cold JC-1 buffer, and JC-1 aggregates (λ excitation/ λ emission = 585 nm/590 nm) and JC-1 monomers (λ excitation/ λ emission = 514 nm/529 nm) were observed by CLSM. To quantify the MMP, after exposure to different treatments, the cells were trypsinized, collected in medium containing JC-1 staining solution (10 μ M), and

incubated in the same environment for 30 minutes. After washing with ice-cold JC-1 buffer, the cells were suspended in 200 μ L of PBS for FC analysis.

TEM

TEM was used to detect the changes in mitochondrial morphology after different treatments to assess ferroptosis induction. HOS cells were seeded overnight into a 6-well plate at a density of 10^5 cells/well to allow adherence and then divided into groups for various different treatments (control, laser alone, PEG-PLGA-IR780 NPs, laser+PEG-PLGA-IR780 NPs, MH-PEG-PLGA-IR780 NPs, and laser+MH-PEG-PLGA-IR780 NPs (IR780: 20 μ g/mL)). Next, the cells were trypsinized, collected, and fixed with 2.5% glutaraldehyde and 1% osmic acid. Then, the cells were dehydrated with a graded ethanol series and acetone, embedded, sliced, and stained with 3% uranyl acetate-lead citrate. Finally, the cells were examined by TEM (JEM-1400 Plus, JEOL, Japan).

LPO and Lipid-ROS measurements

To determine the levels of LPOs and Lipid-ROS, HOS cells (1×10^5 /dish) were seeded into a laser confocal cell- culture dish for 24 h of incubation. Then, the cells were treated differently (control, laser alone, PEG-PLGA-IR780 NPs, laser+PEG-PLGA-IR780 NPs, MH-PEG-PLGA-IR780 NPs, laser+MH-PEG-PLGA-IR780 NPs (IR780: 20 μ g/mL)). Subsequently, the cells were stained with 5 μ M LPO (λ excitation / λ emission = 534 nm/535 nm) or 2 μ M C11-BODIPY (λ excitation/ λ emission = 500 nm/510 nm) for 30 minutes at 37°C in the dark. Next, the cells were washed with PBS to remove the excess LPO and C11-BODIPY. Finally, CLSM was used to observe LPO and Lipid-ROS levels in the cells, which were then trypsinized and collected for FC analysis.

Fe²⁺ detection

FerroOrange (λ excitation/ λ emission = 561 nm/570 nm) was used to detect the level of intracellular Fe²⁺. Briefly, HOS cells were seeded into a laser confocal cell- culture dish at a density of 10^5 cells/well overnight to allow adherence and then treated with laser alone, PEG-PLGA-IR780 NPs, laser+PEG-PLGA-IR780 NPs, MH-PEG-PLGA-IR780 NPs, laser+MH-PEG-PLGA-IR780 NPs (IR780: 20 μ g/mL). Then, the cells were stained with 1 μ M FerroOrange for 30 minutes at 37°C in the dark. Next, the cells were washed with PBS to remove the excess FerroOrange. Finally, the cells were observed by CLSM to detect the intracellular Fe²⁺ levels, and then treated with trypsin, collected in 200 μ L of PBS and detected by FC.

Cell apoptosis assay

Apoptosis was determined by FC using annexin V-FITC/PI staining. Briefly, cells were seeded into 6-well plates (1×10^5 cells/well) and incubated overnight for adhesion. Then, the cells were exposed to laser alone, PEG-PLGA-IR780 NPs, laser+PEG-PLGA-IR780 NPs, MH-PEG-PLGA-IR780 NPs, or laser+MH-PEG-PLGA-IR780 NPs (IR780: 20 μ g/mL). After treatments, the cells were collected, washed twice with ice-cold

PBS, and stained with annexin V-FITC and PI according to the manufacturer's instructions. Finally, the samples were suspended in 200 μ L of PBS and then analysed by FC.

Western blot

After HOS cells were treated according to the different regimens, the cells were lysed with RIPA lysis buffer containing PMSF and phosphatase inhibitor within a specified period of time to extract the total protein in the cells. Protein samples (30 to 50 μ g/lane) were separated on a 10%-12% gel by SDS-PAGE and transferred to polyvinylidene fluoride (PVDF) membranes, which were blocked with 5% skim milk for 1.5 h at room temperature, and then incubated overnight with the corresponding primary antibody (1:1000) at 4°C. Next, the membranes were washed with Tris-buffered saline with Tween-20 (TBST) and incubated with the secondary antibody (1:8000) at 37°C for 1 h. Finally, the reactive protein bands on the membrane were detected with an enhanced chemiluminescence (ECL) detection system and developed on film.

Intracellular ATP level

An ATP assay kit was used to determine the intracellular ATP levels. Briefly, HOS cells were grown in 6-well plates at a density of 10^5 cells/well and incubated overnight for adhesion. After the cells were exposed to laser alone, PEG-PLGA-IR780 NPs, laser+PEG-PLGA-IR780 NPs, MH-PEG-PLGA-IR780 NPs, laser+MH-PEG-PLGA-IR780 NPs (IR780: 20 μ g/mL), the cells were trypsinized and centrifugation (12,000 rpm for 5 minutes) at 4°C. Finally, the cell supernatant was collected for RLU detection with a luminometer equipped with a multimode reader (260-Bio, Thermo Fisher Scientific, USA).

Xenograft tumor model

Thirty male BALB/c nude mice (4 weeks old) were supplied by the Experimental Animal Center of Chongqing Medical University. All animal studies were approved by the Ethics Committee of Chongqing Medical University. The mice were housed with free access to a commercial diet and water under specific pathogen-free conditions. After the mice were acclimated for 1 week prior to initiation of the study, HOS tumor-bearing mice were established by subcutaneous injection of 200 μ L of sterile PBS containing a HOS cell suspension at a density of 10^6 cells/mL. After the tumor volumes reached 50 mm³, different treatments were initiated. Thirty mice were randomized into the following 6 groups: (1) control, (2) laser only, (3) PEG-PLGA-IR780 NPs, (4) laser+PEG-PLGA-IR780 NPs, (5) MH-PEG-PLGA-IR780 NPs, (6) laser+MH-PEG-PLGA-IR780 NPs (laser power: 2 W/cm², 5 minutes of irradiation) (PEG-PLGA concentration: 5 mg/mL, volume of 200 μ L). The tumor volume sizes and mouse weights were measured every 4 days for 16 days after treatment, with the tumor volume calculated according to the following formula: $1/2 \times a^2 \times b$ (where a is the short axis and b is the long axis of the tumor). Mice were sacrificed under anaesthesia on day 14, and the xenograft tumors of each animal were weighed and analyzed.

In order to avoid photothermal effect (PTT) and to ensure only effects due to the PDT treatment, the temperature of the tumor region was monitored during irradiation with a Xenogen IVIS Spectrum imaging

system (PerkinElmer, USA) so that the temperature was always below 42°C. Experiments in vitro was operated on ice.

Haematoxylin-eosin (H&E) and immunohistochemistry (IHC)

After sacrifice, mouse tissues from the xenograft tumors, hearts, livers, spleens, kidneys and lungs were dissected out and fixed in 10% formalin for histopathological studies. After fixation, the tissues were dehydrated in a graded series of ethanol and xylene, embedded in paraffin, cut into sections, and stained with H&E. The expression of PCNA and Ki67 in the xenograft tumor tissues was detected by IHC. Briefly, the paraffin-embedded specimens were separated, fixed with 4% paraformaldehyde, and embedded in paraffin. After embedding, the specimens were discontinuously cut into 4 mm thick sections with a microslicer. Tumor sections were blocked and immunostained with antibodies targeting Ki67 (1:200) or PCNA (1:200). Finally, images were captured using a microscope, and PCNA and Ki67 expression was evaluated by counting the number of positive cells from 5 randomly selected fields in the residual viable tumor tissue among the necrotic areas under a light microscope at a magnification of 200×. Data are presented as the percentage of positive cells.

Biosafety of the MH-PEG-PLGA-IR780 NPs and PDT

To determine the toxicity of the MH-PEG-PLGA-IR780 NPs, they were injected into BALB/c nude mice (PEG-PLGA concentration: 5 mg/mL, volume: 200 µL) that had been randomly divided into 5 groups. Twenty-five mice were euthanized on days 0, 1, 7, 14, and 28 post-injection. The vital organs were collected for H&E staining, and blood samples were sent for the blood index (routine blood and biochemistry) analyses. In addition, the methods of determining the biosafety of MH-PEG-PLGA-IR780 NPs-mediated PDT and the other parallel groups were consistent with the aforementioned methods after the mice were sacrificed at 16 days post-irradiation.

Statistical analysis

All data are expressed as mean ± SD and were analyzed with SPSS 22.0 software. Single Student's t-test and one-way ANOVA were used to determine statistical significance between pairs of groups or three or more groups, respectively. Significance levels are shown as *p < 0.05, **p < 0.01, and ***p < 0.001.

Results

Preparation and characterization of the MH-PEG-PLGA-IR780 NPs

MH-PEG-PLGA-IR780 NPs were prepared using a double-emulsion approach and the physical extrusion method (Scheme 1). The morphology of the obtained NPs was observed by TEM (Figure 1A-B). We found that all of the NPs were uniform in size and monodispersed, and there was a lipid shell on the outside of the NPs wrapped by cell membrane. We further analyze the overall protein components in both the MH and MH-PEG-PLGA NPs by sodium dodecyl sulfate-polyacrylamide gel electrophoresis (SDS-PAGE). As shown in Figure 1C, the expression levels of proteins in the two groups were comparable, which further

confirmed the successful encapsulation of the HOS cell membrane. The particle sizes and zeta potentials of these NPs were measured by DLS, and the average size of MH-PEG-PLGA-IR780 NPs was distributed at approximately 236.8 nm (Figure 1D), which is consistent with the size obtained by TEM. DLS also showed that the average sizes of the PEG-PLGA NPs and PEG-PLGA-IR780 NPs were narrowly distributed and centered at 202.1 nm and 218.2 nm, respectively (Figure S2), suggesting that the resulting average sizes of these NPs would allow them to pass through the tumor endothelial space [28]. Next, to examine the stability of the synthesized NPs, they were placed in either DMEM (10% serum) or PBS at 4°C for one week. Their mean size was measured every day did not change significantly within 7 days (Figure S3), suggesting that the obtained NPs had good stability under physiological conditions. In addition, the zeta potential of the PEG-PLGA NPs and PEG-PLGA-IR780 NPs were -4.62 ± 0.79 mV and -6.70 ± 0.50 mV respectively, while that of the MH-PEG-PLGA-IR780 NPs decreased to -10.09 ± 0.70 mV (Figure 1E), which was possibly caused by the negative charge from cell membrane and the minimization of the electrostatic repulsion of IR780. The negative zeta potential of the MH-PEG-PLGA-IR780 NPs is beneficial for accurate tumor targeting due to a decrease in rapid elimination by the reticuloendothelial system (RES) and prolongation of the time in systemic circulation [29]. The color of the PEG-PLGA NPs and NPs-coated IR780 changed from white to green (Figure 1F). UV-vis spectrum showed that the PEG-PLGA-IR780 NPs and MH-PEG-PLGA-IR780 NPs had a characteristic absorption peak from IR780 at 798 nm, further indicating the successful loading of IR780 compared with the PEG-PLGA NPs, which did not show this characteristic absorption peak (Figure 1G). The absorbance of IR780 changed in a concentration-dependent manner, as determined by UV-vis spectrum, and a calibration curve was constructed (Figures 1H, S4). Finally, the EE and LC of IR780 were calculated to be 67.8% and 3.25 wt%, respectively.

Biosafety assessment of the MH-PEG-PLGA-IR780 NPs

To verify the safety of the MH-PEG-PLGA-IR780 NPs in vitro, a CCK-8 assay was used to examine the effects of a wide range of NPs concentrations (PEG-PLGA: 0.0, 0.2, 0.4, 0.6, 0.8, 1.0 mg/mL) on the cell viability of HOS after 12 h of treatment, and a neutralized concentration of the NPs (PEG-PLGA: 0.4 mg/mL) was used to determine the cell viability at different treatment times (0, 12, 24, 48 h). As shown in Figure 2A-B, the PEG-PLGA NPs had no toxicity to HOS cell, whereas the NPs-wrapped IR780 exhibited mild cytotoxicity at a high NPs concentration (PEG-PLGA ≥ 1.0 mg/mL) which was caused by the weak cytotoxicity of IR780[30]. Additionally, the MH-PEG-PLGA-IR780 NPs (PEG-PLGA: 4 mg/mL, 200 μ L) were intravenously injected into BALB/c nude mice, and blood samples and the major organs (heart, liver, spleen, lung and kidney) were collected after 0, 1, 7, 15, and 28 days post-injection. The routine blood examination and serum biochemical index results showed no significant differences between the sample, and no obvious histopathological changes were observed in the aforementioned vital organs after treatment with the MH-PEG-PLGA-IR780 NPs, indicating acceptable biocompatibility and biosafety in vivo (Figure 2C-D).

Intracellular uptake and deep penetration of the MH-PEG-PLGA-IR780 NPs

To determine whether the MH-PEG-PLGA-IR780 NPs possessed high affinity for HOS cells, the cellular uptake efficiency of the MH-PEG-PLGA-IR780 NPs (labelled with DiI) was explored by CLSM and FC. As shown in Figures 3A, S5, compared with no obvious change of red FL in PEG-PLGA NPs group and a mild increase of red FL in PEG-PLGA-IR780 NPs group, the red FL in the cells coincubated with MH-PEG-PLGA-IR780 NPs increased significantly with the prolonged incubation time, reaching greater than 90% uptake after 4 h of coincubation by the quantitative analyses of FC, indicating that encapsulating the PEG-PLGA-IR780 NPs with the tumor cell membrane could solve the problem of poor affinity of the PEG-PLGA-IR780 NPs for HOS cells. Moreover, hypertension of the tumor sites caused by tumor vascular heterogeneity and the increase in the interstitial pressure further limits the penetration depth and width of NPs in the tumor region [31]. It has been reported that IR780 contained within NPs can achieve surface-to-core penetration of tumor cells [32], but PEG-PLGA-IR780 NPs failed to reveal the anticipated penetration capability. Thus, the following experiments were carried out to evaluate whether the tumor cell membrane was desirable to improve the deep penetration ability of the PEG-PLGA-IR780 NPs, which was implemented by using 3D tumor sphere models to simulate the complex conditions of tumor sites. We cultured 3D tumor spheroids *in vitro* to examine the penetration capability of the MH-PEG-PLGA-IR780 NPs. As shown in Figure 3B, CLSM observations showed that the MH-PEG-PLGA-IR780 NPs (labelled with DiI) could penetrate into the centre of the 3D tumor spheres for uniform distribution throughout the tumor cells, suggesting that the superior penetration depth and width of IR780 in HOS 3D tumor spheroids can be achieved by the homologous targeting from tumor cell membrane.

Homologous targeting facilitated mitochondrial targeting

Due to tumor heterogeneity, the expression levels of surface antigens in the cell membranes responsible for multicellular aggregation formation in tumors are relatively diversified. MH-PEG-PLGA-IR780 NPs exhibit a homologous targeting ability owing to their functionalization by adhesion proteins from the HOS cell membrane. In addition, the homologous targeting of the MH-PEG-PLGA-IR780 NPs to HOS cell line should also have a potential capability of mitochondrial targeting. As shown in Figure 4A, CLSM images showed that the red FL (MH-PEG-PLGA-IR780 NPs) overlapped with the green FL (mitochondria) stained by MitoTracker. The corresponding PC coefficient was determined to be 0.951 for the MH-PEG-PLGA-IR780 NPs, while an unsatisfied co-localization was observed in PLGA-IR780 NPs and PEG-PLGA-IR780 NPs groups, whose PC coefficients were calculated to be 0.231 and 0.303, respectively, suggesting that the MH-PEG-PLGA-IR780 NPs had a high affinity for the mitochondria in HOS cells, which would potentially promote PDT performance because mitochondria are susceptible to ROS-mediated cytotoxicity.

Next, we wanted to verify whether the mitochondrial targeting capacity of the MH-PEG-PLGA-IR780 NPs to HOS cell line was achieved by its homologous targeting. It has been reported that 4T1 and A549 cells are sensitive to the mitochondria targeting ability of NPs wrapping IR780[3, 33], so both of these cells were coincubated with MH-PEG-PLGA-IR780 NPs for 4 h. However, CLSM images demonstrated almost no red FL overlap with green FL from MitoTracker in A549 (PC = 0.128) and 4T1 (PC = 0.155) cells. Meanwhile, other OS cell lines (MG63, 143B, K7M2) and human osteoblasts (hFOB 1.19) were chosen for incubation

with the MH-PEG-PLGA-IR780 NPs for 4 h followed by CLSM imaging, and only a suboptimal overlap (PC = 0.426) was found between the green FL and red FL in 143B cells, which may be due to the 143B cell was also known as a HOS cell line with k-ras oncogene transformation [34]. Poor co-localization was observed in the MG63 (PC = 0.125), K7M2 (PC = 0.185) and HFOB 1.19 (PC = 0.122) cells (Figure 4B), indicating that the PEG-PLGA-IR780 NPs wrapped by tumor cell membranes have a potential ability to achieve mitochondrial targeting in only homologous tumor cells. Furthermore, the immune escape capability of different NPs was detected in RAW 264.7 murine macrophage-like cells. RAW 264.7 cells were incubated with various NPs for 4 h and then imaged with CLSM, the red FL in PEG-PLGA NPs group was brighter than PEG-PLGA-IR780 NPs group, while the MH-PEG-PLGA-IR780 NPs could avoid being swallowed by RAW 264.7 cells and showed least intense red FL (Figure S6), indicating that coating cancer cell membrane could endow the NPs with antiphagocytic capability of RAW 264.7 cells possibly due to the reduction in immune clearance. In conclusion, the MH-PEG-PLGA-IR780 NPs achieved mitochondrial targeting of HOS cell with the assistance of homologous targeting and immune evasion ability by the virtue of ligand receptors on the cell membrane.

In vivo biodistribution by FL and PA Imaging

IR780 has been used as a fluorescent probe to impart the MH-PEG-PLGA-IR780 NPs with NIR FL (λ excitation/ λ emission = 745 nm/820 nm) and PA (wavelength = 780nm) imaging capabilities to evaluate the distribution of tumor accumulation and the biodistribution of MH-PEG-PLGA-IR780 NPs in vivo [27]. MH-PEG-PLGA-IR780 NPs were intravenously injected into HOS tumor-bearing mice to detect the distribution of the MH-PEG-PLGA-IR780 NPs in vivo after prolonged periods of times. As shown in Figures 5A, 5C, the FL signal began to aggregate within the tumor region in a time-dependent manner and reached a peak at 6 h post-injection. Thus, FL intensities of the harvested vital organs and tumors were measured after 6 h post-injection for ex vivo FL imaging to confirm the NPs biodistribution, and it was found that the FL intensities in tumors were higher than those of the heart, liver, spleen and kidney, but lower than that in the lung [35] (Figures 5B, 5D), suggesting that the superior targeting properties of MH-PEG-PLGA-IR780 NPs in vivo.

In biological tissues, PA imaging has superior contrast, resolution and penetration, enabling the integration of diagnosis and treatment by determining the precise location of the drugs in the targeted region of the tumor [36]. Therefore, PA imaging was recorded to further clarify the distribution of the MH-PEG-PLGA-IR780 NPs in vivo. Generally, an obvious PA signal intensity began to focus on the tumor region at 1 h post-injection, reached a peak at 6 h post-injection (Figure 5E-F). These results were consistent with those from FL imaging. In conclusion, both the results of FL and PA imaging verified that the MH-PEG-PLGA-IR780 NPs may effectively accumulate in tumor region in vivo, laying a foundation for further tumor diagnostic imaging and targeting therapy.

Homologous and mitochondrial targeting enhanced PDT performance

After tumor/mitochondrial targeting was achieved by homologous targeting, a CCK-8 assay was used to estimate the antitumor efficacy of PDT in vitro. As shown in Figure 6A, compared to no obvious change in

the control, laser alone, and single NPs without NIR irradiation groups, the MH-PEG-PLGA-IR780 NPs exposed to laser (targeted PDT group) decreased the cell viability of HOS in a IR780 dose-dependent manner at power densities of 1 W/cm² and 1.5 W/cm², while laser+PEG-PLGA-IR780 NPs (PDT without targeting) showed weak photoinduced cytotoxicity on HOS cells. Considering that the use of IR780 alone at a concentration greater than 30 µg/mL had mild cytotoxic effects on HOS cells after 4 h of coincubation, 20 µg/mL MH-PEG-PLGA-IR780 NPs was selected to examine the efficacy and specific mechanism of MH-PEG-PLGA-IR780 NPs-mediated PDT in the following experiments.

First, the morphology of the mitochondria was observed by CLSM. As shown in Figure 6B, compared with the physiological morphology of mitochondria in the other five groups, mitochondrial fragmentation was found in HOS cells upon treatment with the targeted PDT, which could further lead to mitochondrial dysfunction. In addition, PDT performance was detected by DCFH-DA, a probe that detects intracellular ROS generation by showing green FL. As shown in Figure 6C, compared with no significant alteration in the control, laser alone and two single NPs groups, PDT without targeting showed mild green FL, while the targeted PDT produced strong green FL in HOS cells under 808 nm NIR irradiation (1.5 W/cm²), which was accompanied by typical morphological features of apoptotic cell, indicating the initiation of cell death. Moreover, we quantitatively analyzed the percentage of intracellular ROS in cells by FC, and compared with the parallel groups, the amount of ROS produced by PDT without homologous and mitochondrial targeting was 44.60%, while this value after treatment with targeted PDT was significantly increased to 98.97% (Figure 6D). ATP, one of the most important energy supply substances, is mainly derived from mitochondrial metabolism [37], and plays a key role in tumor proliferation and DNA replication. It has been reported that ATP depletion causes tumor cells to be more sensitive to PDT [38]. To demonstrate the changes in ATP contents after different treatments, a calibration curve of ATP was constructed (Figure S7). And as shown in Figure 6F, compared with the other five groups, only PDT with homologous and mitochondrial targeting treatment led to a significant decrease in the intracellular ATP content. In conclusion, these results suggested that homologous and mitochondrial targeting could improve PDT performance by increasing intracellular ROS production and inhibiting ATP synthesis.

Homologous and mitochondrial targeting synergistically induced apoptosis and ferroptosis.

Cell death is a fundamental biological process generally including necrosis, apoptosis, autophagy and ferroptosis. The synergistic induction of multiple death modes in combination with tumor therapy is an effective strategy to improve PDT performance [18]. We next set out to investigate the main cell death modes of the dual-targeting nanoplatfrom-mediated PDT. Therefore, before NIR irradiation, HOS cells were pretreated with multiple inhibitors of cell death pathways for 24 h, including an apoptosis inhibitor (z-VAD-FMK), a necrosis inhibitor (Nec-1), an autophagy inhibitor (Baf-A1), a ferroptosis inhibitor (Fer-1) and a general ROS scavenger (NAC). As displayed in Figure S8, the CCK-8 assay showed that compared with the significant inhibitory effect of cell viability by targeted PDT, the viability of HOS cells increased after pretreatment with each inhibitors (excepting Baf-1) followed targeted PDT treatment to different degrees, but NAC, Fer-1 and z-VAD-FMK significantly protected HOS cells from photoinduced cytotoxicity caused by PDT, while Baf-1 promoted the inhibitory effects of PDT on HOS cell viability, suggesting that

in addition to apoptosis, ferroptosis was another key cell death mode mediated by MH-PEG-PLGA-IR780 NPs-induced PDT, and autophagy acted as a presurgical role in PDT treatment.

Therefore, we hypothesized that mitochondrial dysfunction accomplished by homologous targeting by targeted PDT treatment was desirable to synergistically induce mitochondrial apoptosis (endogenous apoptosis) and ferroptosis to kill HOS cells. Then, we sought to further verify this assumption and explore underlying cell death mechanism. First, we measured cell apoptosis by FC using annexin V-FITC/PI double staining analysis. As shown in Figure 7A-B, the control, NIR irradiation alone, PEG-PLGA-IR780 NPs and MH-PEG-PLGA-IR780 NPs alone without irradiation groups did not induce obvious apoptosis in HOS cells. The apoptosis rate of HOS cells induced by PDT without targeting was 25.05%, while the targeted PDT treatment increased the cell apoptosis rate to 64.57%. Then, considering the important role of MMP ($\Delta\psi_m$) in mitochondrial apoptosis, we measured the $\Delta\psi_m$ with the fluorescent probe JC-1. During the mitochondrial apoptotic process, the mitochondrial membranes were disrupted with the depolarization of the $\Delta\psi_m$, and the mitochondrial depolarization was verified by the decrease in the red to green FL intensity ratio in JC-1 assay. As shown in Figure 7C-E, HOS cells were stained with JC-1 after different treatments. Compared with no obvious change in the control, single NIR irradiation, and two NPs alone groups, we observed that laser+PEG-PLGA-IR780 NPs treatment exhibited a mild decrease in red FL and a weak increase in green FL, and these changes were more prominent after treatment with the laser+MH-PEG-PLGA-IR780 NPs. Furthermore, to further investigate the underlying mechanisms of the pro-apoptotic effects of the nanoplatform-mediated PDT, the expression levels of apoptosis-related proteins were assessed by western blot. It was found that laser+MH-PEG-PLGA-IR780 NPs treatment significantly increased the expression of cytochrome c, cleaved caspase-7, cleaved caspase-9, pro-apoptotic protein Bax, which was accompanied by obvious downregulation of the anti-apoptotic protein Bcl-2 which ultimately led to the marked upregulation of cleaved caspase-3. However, the expression levels of these apoptosis-related proteins revealed no prominent change in the control, single NIR irradiation, two NPs alone without irradiation groups, and PDT without targeting group, which produced unstable pro-apoptotic effects (Figure 7F-L).

Intriguingly, the dual-targeting (MH-PEG-PLGA-IR780 NPs) constructed in our study have the innate advantage to induce ferroptosis under NIR irradiation. On the one hand, the increase in intracellular ROS and the large number of polyunsaturated fatty acids (PUFAs) in the cell membrane were found to be the key drivers of ferroptosis [39], which are susceptible to oxidation to form LPOs. On the other hand, mitochondrial targeting-mediated ferroptosis has been reported to be an emerging strategy for cancer therapy [40]. To further examine the level of ferroptosis, LPOs and Lipid-ROS have been recognized as crucial biomarkers of ferroptosis to impair cell structure and integrity, and both of which were detected by liperfluo and C11-BODIPY, respectively [41]. As shown in Figure 7M-N, CLSM images showed that the contents of both LPOs and lipid-ROS of HOS cells were significantly increased, as indicated by the significant increase in green FL intensity, after laser+MH-PEG-PLGA-IR780 NPs treatment compared with no remarkable alteration in the control, laser alone and single two NPs without irradiation groups. In addition, the slight green FL was observed in laser+PEG-PLGA-IR780 NPs treatment which was consistent with the mild cell apoptosis induced by this treatment group. Moreover, quantitative analysis via FC

illustrated the same phenomenon (Figure 7O-R), indicating that this dual-targeting-based theranostic nanoplatform had superior advantages on inducing ferroptosis under NIR irradiation, and the inadequate ability of PEG-PLGA-IR780 NPs combined with NIR irradiation to induce ferroptosis may be due to the lack of mitochondrial targeting and PUFAs. Mitochondria shrinkage is another important character of death phenotype in ferroptosis [42, 43]. The results of TEM also demonstrated that the morphology of mitochondria treated with targeted PDT became round, dwindled in size, reduced or disappeared mitochondrial cristae, and exhibited structural damage, while mitochondria in the other five groups showed a normal physiological morphology (Figure 7S). Therefore, we confirmed that the emerging nanoplatform-mediated PDT could significantly synergistically induce HOS cell apoptosis and ferroptosis by homologous and mitochondrial targeting.

MH-PEG-PLGA-IR780 NPs-mediated PDT promoted ferroptosis by inactivating GPX4 and accumulating Fe²⁺ by ferritinophagy

Three of the major factors that affect ferroptosis are tailored lipid metabolism, redox-active iron (Fe²⁺) and the inactivation of GPX4, a lipid repair enzyme that is responsible for preventing LPO cytotoxicity and maintaining membrane lipid bilayer homeostasis [44]. To further investigate the specific mechanism of ferroptosis induced by MH-PEG-PLGA-IR780 NPs-mediated PDT, we first detected the protein expression of GPX4 by western blot, as shown in Figure 8A-D, GPX4 expression was significantly downregulated by the laser+MH-PEG-PLGA-IR780 NPs treatment, while the other five treatments did not achieve the identical effect. SLC7A11 and SLC3A2 are subunits of system X_C⁻, a glutamate/cysteine antiporter, which are responsible for maintaining the cellular antioxidant environment, and the low expression of both of these subunits would induce the passivation of GPX4, preventing ROS production during ferroptosis [45]. Unsurprisingly, compared with the parallel treatment groups, PDT without targeting showed no influence on either SLC7A11 or SLC3A2 protein expression. However, SLC3A2 protein expression was significantly downregulated by the laser+MH-PEG-PLGA-IR780 NPs treatment, and the protein expression of SLC7A11 was only mildly decreased in this group. In conclusion, the downregulation of both SLC3A2 and SLC7A11 resulted in the deactivation of GPX4.

In addition, excessive accumulation of redox-active iron (Fe²⁺) in cells promotes the production of excessive hydroxyl radicals because of the Fenton reaction ($\text{Fe}^{2+} + \text{H}_2\text{O}_2 \rightarrow \text{Fe}^{3+} + (\text{OH})^- + \cdot\text{OH}$). Hydroxyl radicals ($\cdot\text{OH}$), another ROS, are able to oxidize PUFAs, producing LPOs. Thus, we measured the intracellular Fe²⁺ generation capability of dual-targeting nanoplatform-associated PDT by FerroOrange (Japan, colleagues). As shown in Figure 8E, CLSM analysis showed that compared with the parallel groups, the treatment of targeted PDT significantly increased the intracellular Fe²⁺ levels, as shown by the strong red FL intensity. The quantitative analysis of FC also confirmed that the percentage of intracellular Fe²⁺ by the targeted PDT treatment raised to 65.11%, which was consistent with the above findings (Figure 8F-G). It has been reported that nuclear receptor coactivator 4 (NCOA4)-mediated ferritinophagy increases the level of redox-active iron in the cytoplasm and induces ferroptosis by degrading ferritin [46-48]. The proteins involved in iron storage are Ferritin heavy chain (FTH) and Ferritin light chain (FTL). To

further analyse whether the specific molecular mechanism of the obtained increase in intracellular Fe^{2+} level was associated with NCOA4-mediated ferritinophagy, the protein expression levels of NCOA4, FTH and FTL were determined by western blot. As shown in Figure 8H-K, accompanied by no obvious changes in the control, laser alone, and NPs without irradiation groups, PDT without targeting treatment showed a mild increase in NCOA4 expression and a weak reduction in FTH expression, while the expression of NCOA4 was significantly elevated and the expression of FTH and FTL were remarkably declined in the laser+MH-PEG-PLGA-IR780 NPs group. In addition, the levels of FTH and FTL expression were further confirmed by immunofluorescence (IF) assay. Generally, consistent with western blot results, the laser+MH-PEG-PLGA-IR780 NPs showed significant green FL intensity from NCOA4, which was brighter than that in the other five groups, and an arresting feeble red FL intensities of FTH and FTL was discovered in laser+MH-PEG-PLGA-IR780 NPs treatment which were remarkably lower than those of the control, single NIR irradiation, and two NPs without irradiation groups, while PDT without targeting showed limited changes in the FL intensities of NCOA4, FTH and FTL (Figure 8L). In conclusion, we demonstrated that this dual-targeting-associated theranostic nanoplatform can not only decrease the activity of GPX4 by the inhibiting system Xc^- transport, but also promote the accumulation of Fe^{2+} by activating NCOA4-mediated ferritinophagy to degrade ferritin, synergistically inducing ferroptosis in HOS cells.

Antitumor efficacy in vivo

Based on the effective induction of cell apoptosis and ferroptosis by MH-PEG-PLGA-IR780 NPs-mediated PDT in vitro, we examined whether a similar inhibitory effect could occur in a xenograft model. HOS bearing-mice were subcutaneously divided into six groups for different treatments: (1) control (PBS), (2) laser alone, (3) single PEG-PLGA-IR780 NPs, (4) laser+PEG-PLGA-IR780 NPs, (5) single MH-PEG-PLGA-IR780 NPs, and (6) laser+MH-PEG-PLGA-IR780 NPs. The tumor areas were irradiated with an NIR laser (808 nm, 2 W/cm², 5 minutes) after 6 h post-injection in the appropriate groups considering PA and FL imaging results. After different therapies, the representative images of the mice before sacrifice and tumor visualization were captured, and tumor volumes were measured every 4 days over 16 days to monitor different treatment outcomes (Figure 9A-B, S9), we found the tumor growth in the PBS and laser alone groups were increased to closely 6.82-fold and 6.13-fold compared with the original tumor volumes, and the tumor volumes of single two NPs groups presented a 5.25-fold and 4.78-fold increase, respectively, and laser+PEG-PLGA-IR780 NPs group inhibited tumor growth suboptimally due to its lack of targeting (3.07-fold increase). In contrast, laser+MH-PEG-PLGA-IR780 NPs group almost completely inhibited the growth of tumors, demonstrating a significant tumor inhibition effect in vivo, which is consistent with the photoinduced cytotoxicity in vitro. Subsequently, the trend in tumor size and weight ex vivo were measured and shown in Figure 9C-D. No obvious change in mice weights between the control and treated groups were observed during the experimental period (Figure S10).

Furthermore, we also evaluated the expression of proliferation markers, including PCNA and Ki67, to further validate the inhibitory effects of different treatments on tumor growth. The expression levels of PCNA and Ki67 in tumor specimens measured by IHC from the laser+PEG-PLGA-IR780 NPs group were

lower than those in the control, laser alone, and single two NPs groups, while the laser+MH-PEG-PLGA-IR780 NPs group showed the lowest expression. Specimens from the xenograft tumors were stained with H&E after mouse sacrifice, as tumor necrosis (karyopyknosis, karyorrhexis, and karyolysis) is a crucial criterion for evaluating the response to various treatments in HOS cells [49]. We found that the specimens from the two PDT groups showed different degrees of necrosis, while the laser+MH-PEG-PLGA-IR780 NPs group were associated with the most severe necrosis (Figures 9E, S11). To detect the therapeutic biosafety of PDT in vivo, H&E staining of the main organs (heart, liver, spleen, lung and kidney) was performed at the end of the various treatments, and routine blood and biochemistry analysis also showed no significant differences among the various groups (Figure S12). In addition, no apparent histopathological abnormalities were observed via H&E staining (Figure S13). Taken together, these findings indicated that MH-PEG-PLGA-IR780 NPs could enhance PDT performance in a xenograft model with high therapeutic potential and biosafety.

Ferroptosis-promoted PDT performance

As a new mode of RCD, ferroptosis is desirable to improve the production of free radicals via the Fenton reaction, resulting in an increase in ROS-mediated oxidative damage to cellular constituents and ensuring the high efficiency of PDT. To further determine whether ferroptosis induced by targeted PDT treatment could enhance the original killing characteristics of PDT in vivo, we administered PDT targeted therapy to HOS xenograft tumor-bearing mice after a combination injection of MH-PEG-PLGA-IR780 NPs and Deferoxamine (DFO), a ferroptosis inhibitor that functions by chelating iron. The tumor size was measured every 4 days over 16 days in the above treatment groups, and it was found that compared with the significant inhibitory effects of the targeted PDT treatment, DFO weakened tumor growth in the xenograft model by inhibiting ferroptosis. Visualization and the weights of the representative tumors *ex vivo* followed a similar trend, with no significant alterations in body weight (Figure 10A-D). These results indicated that ferroptosis activation allowed the new nanoplatform-mediated PDT to be capable of promoting the antitumor effects of PDT in vivo.

In vitro, we further clarified whether the inhibition of ferroptosis could protect HOS cells from the photoinduced cytotoxic effects of the targeted PDT treatment. HOS cells were pre-incubated with DFO for 24 h followed by targeted PDT treatment. Since this nanoplatform-mediated PDT induced ferroptosis was also dependent on tailored lipid peroxidation, HOS cells were pretreated with another ferroptosis inhibitor Fer-1 for 24 h before targeted PDT intervention. As shown in Figures 10E-M, both DFO and Fer-1 inhibited the promoting effects of targeted PDT on the levels of intracellular ROS, lipid-ROS and LPOs, showing weaker green FL intensity by CLSM, which is in accordance with the results obtained by FC. Considering that DFO inhibited ferroptosis by depleting intracellular Fe^{2+} and indirectly blocking lipid peroxidation, the content of intracellular Fe^{2+} was detected by FerroOrange, and as shown in Figure S14, both CLSM images and FC analyses showed the same conclusion. Compared with the laser+MH-PEG-PLGA-IR780 NPs group, DFO significantly inhibited the production of intracellular Fe^{2+} during PDT. In summary, these results indicated that effective blockade of ferroptosis might protect HOS cells from the cytotoxic effects of intracellular ROS, Lipid-ROS and LPOs induced by targeted PDT. Additionally, the CCK-

8 assay showed that the pretreatment of Fer-1 or DFO followed targeted PDT could effectively increase the cell viability of HOS (Figure 10N). Moreover, to further investigate the relationship and the potential signaling pathways between the targeted PDT-induced apoptosis and ferroptosis, as shown in Figure 10O-W, both Fer-1 and DFO attenuated targeted PDT-mediated apoptosis by inhibiting Cytochrome c and Bax protein levels, which is consistent with the upregulation of Bcl-2 protein expression, ultimately resulting in a decreased protein level of cleaved caspase-3. Finally, annexin V-FITC/PI double staining analysis showed the cells pretreated with Fer-1 or DFO followed by targeted PDT treatment exhibited marked inhibition of the total apoptosis rate of HOS cells compared with targeted PDT without ferroptosis inhibitors (Figure 10X-Y). Taken together, these results indicated that the induction of ferroptosis by the theranostic nanoplatfrom-mediated PDT could contribute to the PDT-mediated apoptosis and inhibit tumor growth in mouse xenografts.

Discussion

OS is the most common malignant bone tumor in children and adolescents. As an emerging treatment showing noninvasiveness, high selectivity and few side effects, PDT has been used in the clinical treatment of superficial tumors such as those in skin cancer [50]. Studies have also reported that PLGA-coated photosensitizers can enhance PDT performance to different cancers, such as breast cancer and prostate cancer [27, 38, 51]. However, few studies have been conducted to examine the combination of nano-scale drug-delivery systems and PDT in OS treatment. The lack of PDT targeting to OS tumors and the single death mode featuring unstable therapeutic effects severely limits the PDT efficiency. As a potential method, ligand-receptor binding may solve the problem of poor tumor targeting caused by immune rejection of the mononuclear phagocyte system (MPS) [52], but no specific and effective receptor has been found for clinical treatment of the OS[4, 53]. In this study, tumor cell membranes were used to endow NPs with homologous targeting and immune escape abilities, which showed tumor targeting in vivo and vitro to OS through ligand receptors on the surface of the cell membranes. Modification of NPs using biofilms such as erythrocyte and macrophage membranes could endow NPs with some of the characteristics of the original cells [54, 55]; for example, coating NPs with red blood cell membranes could their extend blood circulation time[56]. However, compared with tumor cell membranes, positive tumor targeting cannot be implemented due to the lack of targeting molecules on the surface of other types of cell membranes [13, 14, 57].

In addition, mitochondrial dysfunction plays a key role in the regulation of tumor cell death. (i) The mitochondria of tumor cells have a higher membrane potential ($\Delta\psi_m$) and produce less ATP, which makes the mitochondria of tumor cells more sensitive to mitochondrial targeted drugs [58]. (ii) Mitochondrial dysfunction can cause depolarization of the $\Delta\psi_m$, promote the release of cytochrome c and activate the endogenous apoptosis pathway mediated by cleaved caspase-9, cleaved caspase-7 and cleaved caspase-3[49, 59]. (iii) ROS act as a "double-edged sword" to cause damage to proteins, lipids and oxidative phosphatases [60], which are produced by PDT and mainly come from mitochondria. As a photosensitive agent, IR780 can target tumor mitochondria due to the activation of organic anion-transporting polypeptides (OATPs) in tumor cells, which contribute to the transmembrane transport of

IR780 during tumor phagocytosis, and finally allow diffusion of the NPs into the tumor core [9, 61, 62]. Therefore, we constructed the tumor/mitochondrial targeting NPs vector MH-PEG-PLGA-IR780 by combining homologous targeting capacity from the HOS cell membrane and mitochondrial targeting capacity from IR780. According to the obtained CLSM and FC results, MH-PEG-PLGA-IR780 NPs had superior tumor/mitochondrial targeting to HOS cells and excellent penetration depth into 3D tumor spheroids, laying a foundation for improving the performance of PDT. However, there are a large number of ligands and receptors on the surface of the tumor cell membranes which might cause biosafety risks *in vivo*, so we performed routine blood, biochemistry analysis and H&E staining of vital organs (heart, liver, spleen, lung and kidney) at 1, 7, 14, and 28 days after the injection of MH-PEG-PLGA-IR780 NPs in BALB/c nude mice. The results showed that the MH-PEG-PLGA-IR780 NPs had no toxicity or side effects *in vivo*, corroborating the results from the CCK-8 assay *in vitro*, suggesting that the MH-PEG-PLGA-IR780 NPs not only had excellent targeting properties to HOS cells but also showed perfect biosafety *in vivo* and *in vitro*.

Inducing a single cell death mode may fail to eradicate tumor cells due to the complex tumor microenvironment and tumor heterogeneity [16]. Fortunately, the increase in intracellular ROS caused by dual-targeting theranostic nanoplatfrom-mediated PDT resulted in a close relationship between cell apoptosis and ferroptosis. Our results demonstrated that MH-PEG-PLGA-IR780 NPs-mediated PDT could significantly induce HOS cells apoptosis and ferroptosis, and the specific mechanism was further explored. The induction of apoptosis involves two classical pathways: the death receptor pathway (extrinsic pathway) and the mitochondrial pathway (intrinsic pathway) [63]. In the mitochondrial apoptotic pathway, a decrease in the $\Delta\psi_m$ leads to an increase in mitochondrial membrane permeability, which further results in the release of cytochrome c from the mitochondria into the cytoplasm. In the cytoplasm, cytochrome c initiates the activation of caspases and eventually induces cell apoptosis. The release of cytochrome c is prevented by the anti-apoptotic protein Bcl-2. Furthermore, we observed a decrease in Bcl-2 expression accompanied by an increase in the expression of the pro-apoptotic protein Bax, cytochrome c, cleaved caspase-9, cleaved caspase-7 and cleaved caspase-3 by western blot. These results demonstrated that it is the activation of the mitochondrial apoptotic pathway that resulted in the cell apoptosis by the dual-targeting theranostic nanoplatfrom-mediated PDT. In addition, the nanoplatfrom-mediated PDT induced ferroptosis mainly resulted from two molecular mechanism. On the one hand, the excessive accumulation of intracellular Fe^{2+} derived from the activation of NCOA4-mediated ferritinophagy and the degradation of FTH protein and FTL protein. On the other hand, the inactivation of GPX4 by inhibiting the X_C^- system (SLC7A11/ SLC3A2), indicating a compromised cellular antioxidant defense system. Finally, both of these aspects led to the excessive accumulation of intracellular LPOs and lipid-ROS to impair cell structure and integrity. Due to the distinct differences between ferroptosis and apoptosis, compared with the single cell death induction, the simultaneous induction of apoptosis and ferroptosis was expected to overcome the problems of tumor heterogeneity and improve PDT performance. We also demonstrated MH-PEG-PLGA-IR780 NPs-mediated PDT could significantly inhibit tumor growth in mice with HOS xenograft tumors without toxicity or side effects to the vital organs, which is consistent with the prominent photoinduced cytotoxicity *in vitro*.

Fortunately, the excessive accumulation of redox-active iron is attributed to ferroptosis induction, which has the unique advantage of producing oxygen free radicals to induce cell apoptosis to kill tumors through the Fenton reaction in turn [26, 64]. Fe^{2+} and Fe^{3+} are the main oxidation-reduction states of redox-active free iron, and the former is more important in the redox environment in tumor cells [65, 66]. CLSM images and FC analyses demonstrated that MH-PEG-PLGA-IR780 NPs-mediated PDT increased the level of intracellular Fe^{2+} . To further investigate the promotional or antagonistic role of ferroptosis in mediating apoptosis in HOS cells after the treatment with the nanoplatform-mediated PDT, we assessed cell viability and apoptosis after blocking ferroptosis with Fer-1 and DFO. Our results showed after pretreatment with ferroptosis inhibitors Fer-1 and DFO in HOS cells followed targeted PDT, the cell apoptosis rate and cell viability were significantly inhibited. In addition, DFO and MH-PEG-PLGA-IR780 NPs were codelivered to HOS tumor-bearing mice followed NIR irradiation, and the inhibition of ferroptosis via iron chelation significantly reduced the performance of MH-PEG-PLGA-IR780 NPs-mediated PDT in suppressing tumor growth compared to the group without DFO treatment, these results suggested that ferroptosis played a key role as a “death switch” in dual-targeting theranostic nanoplatform-mediated PDT.

Conclusion

In summary, we successfully constructed an emerging nanoplatform (MH-PEG-PLGA-IR780 NPs) with coupled tumor targeting with mitochondrial targeting, and combined this with an NIR irradiation to synergistically induce apoptosis and ferroptosis and improve PDT efficiency in vitro and in vivo. Because of the superior FL/PA imaging performance, this nanoplatform is desirable for precise tumor diagnosis and therapy. In addition, our results suggest that the underlying mechanisms of apoptosis and ferroptosis are initiated by the mitochondrial apoptotic pathway, excessive accumulation of Fe^{2+} and inactivation of GPX4. Finally, blocking ferroptosis inhibited PDT-induced apoptosis by decreasing intracellular ROS and inhibiting the mitochondrial apoptotic pathway, suggesting that ferroptosis could promote the efficiency of PDT in a dual-targeting-associated theranostic nanoplatform.

Abbreviations

OS: osteosarcoma; PDT: photodynamic therapy; ROS: reactive oxygen species; PA: photoacoustic; FL: fluorescence; $\Delta\psi_m$: mitochondrial membrane potential; LPOs: lipid peroxides; GPX4: glutathione peroxidase4; Fer-1: ferrostatin-1; DFO: deferoxamine; CLSM: laser confocal scanning microscopic; FC: flow cytometry; TEM: transmission electron microscopy.

Declarations

Ethics approval

All animal studies were approved by the Ethics Committee of Chongqing Medical University.

Consent for publication

Not applicable.

Availability of data and materials

The datasets used and analyzed during the current study are available from the corresponding author on reasonable request.

Conflict of Interest

The authors declare no conflict of interest.

Funding

This work was supported by the National Natural Science Foundation of China (No. 82072976), Chongqing Science & Technology Commission (No.cstc2019jcyj-msxmX0358, No. cstc2019jcyj-msxmX0853), and the General Basic Research Project from Ministry of Education Key Laboratory of Child Development and Disorders (No. GBRP-202117).

Authors' contributions

YW, LZ, ZXQ, and YSO were responsible for the experimental design. WY, LZ, ZYC, FBZ, TH, YC, and LH performed experiments. YW, GSZ, and YZ performed the data analyses. YW, GSZ, and YZ participated in the discussion and interpretation of the data. YW, LZ, ZXQ, and YSO created the figures and wrote the manuscript. ZGW, ZXQ, YSO, and YZ were responsible for the funding application and the supervision and management of the project. All authors have contributed to and approved the final manuscript.

References

1. Siegel HJ, Pressey JG. Current concepts on the surgical and medical management of osteosarcoma. *Expert Rev Anticancer Ther.* 2008;8:1257.
2. Zhao C, Tong Y, Li X, Shao L, Chen L, Lu J, et al. Photosensitive nanoparticles combining vascular-independent intratumor distribution and on-demand oxygen-depot delivery for enhanced cancer photodynamic therapy. *Small.* 2018; 1703045.
3. Liang Z, Dong W, Ke Y, Sheng D, Yu C. mitochondria-targeted artificial "nano-RBCs" for amplified synergistic cancer phototherapy by a single NIR irradiation. *Adv Sci.* 2018;5:1800049.
4. Corre I, Verrecchia F, Crenn V, Redini F, Trichet V. The osteosarcoma microenvironment: A complex but targetable ecosystem. *Cells.* 2020;15(4):976. 9.
5. Shibue T, Weinberg RA. EMT, CSCs, and drug resistance: the mechanistic link and clinical implications. *Nat Rev Clin Oncol.* 2017;14(10):611–29.

6. Wang K, Zhang Y, Wang J, Yuan A, Sun M, Wu J, et al. Self-assembled IR780-loaded transferrin nanoparticles as an imaging, targeting and PDT/PTT agent for cancer therapy. *Sci Rep*. 2016;6:27421.
7. Tan X, Luo S, Long L, Wang Y, Wang D, Fang S, et al. Structure-guided design and synthesis of a mitochondria-targeting near-infrared fluorophore with multimodal therapeutic activities. *Adv Mater*. 2017;29:1704196.
8. Wang Y, Liu T, Zhang E, Luo S, Tan X, Shi C. Preferential accumulation of the near infrared heptamethine dye IR-780 in the mitochondria of drug-resistant lung cancer cells. *Biomaterials*. 2014;35:4116–24.
9. Zhang E, Chao Z, Su Y, Cheng T, Shi C. Newly developed strategies for multifunctional mitochondria-targeted agents in cancer therapy. *Drug Discov Today*. 2011;16(3–4):140–6.
10. Yue C, Liu P, Zheng M, Zhao P, Wang Y, Ma Y, et al. IR-780 dye loaded tumor targeting theranostic nanoparticles for NIR imaging and photothermal therapy. *Biomaterials*. 2013;34:6853–61.
11. Xm A, Yz B, Hf A, Ws A, Ying CA, Bo CC, et al. Integration of immunogenic activation and immunosuppressive reversion using mitochondrial-respiration-inhibited platelet-mimicking nanoparticles. *Biomaterials*. 2020;232:119699.
12. Li X, Wang X, Zhao C, Shao L, Lu J, Tong Y, et al. From one to all: self-assembled theranostic nanoparticles for tumor-targeted imaging and programmed photoactive therapy. *J Nanobiotechnology*. 2019;17:23.
13. Rao L, Bu LL, Cai B, Xu JH, Li A, Zhang WF, et al. Cancer cell membrane-coated upconversion nanoprobe for highly specific tumor imaging. *Adv Mater*. 2016;28:3460–6.
14. Luk BT, Zhang L. Cell membrane-camouflaged nanoparticles for drug delivery. *J Control Release*. 2015;220:600–7.
15. Chilakamarthi U, Giribabu L. Photodynamic therapy: past, present and future. *Chem Rec*. 2017;17(8):775–802.
16. Castano AP, De Midova TN, Hamblin MR. Mechanisms in photodynamic therapy: part two—cellular signaling, cell metabolism and modes of cell death. *Photodiagnosis Photodyn Ther*. 2005;2:1–23.
17. Lihong S, Qian L, Mengmeng H, Ya G, Ruihao Y, Lei Z, et al. Light-activatable Chlorin e6 (Ce6)-imbedded erythrocyte membrane vesicles camouflaged Prussian blue nanoparticles for synergistic photothermal and photodynamic therapies of cancer. *Biomater Sci*. 2018;24(11):2881–95. 6).
18. Melamed JR, Edelstein RS, Day ES. Elucidating the fundamental mechanisms of cell death triggered by photothermal therapy. *ACS Nano*. 2015;9:6–11.
19. Zhou Z, Song J, Nie L, Chen X. Reactive oxygen species generating systems meeting challenges of photodynamic cancer therapy. *Chem Soc Rev*. 2016;21(23):6597–626. 45.
20. Easwaran H, Tsai HC, Baylin SB. Cancer Epigenetics: Tumor heterogeneity, plasticity of stem-like States, and drug resistance. *Mol Cell*. 2014;54:716–27.

21. Holohan C, Schaeybroeck SV, Longley DB, Johnston PG. Longley DB and Johnston PG. Cancer drug resistance: an evolving paradigm. *Nature*. 2013;13:714–24.
22. Dixon SJ, Lemberg KM, Lamprecht MR, Skouta R, Zaitsev EM, Gleason CE, et al. Ferroptosis: an iron-dependent form of nonapoptotic cell death. *Cell*. 2012;25(5):1060–72. 149.
23. Hangauer MJ, Viswanathan VS, Ryan MJ, Bole D, Eaton JK, Matov A, et al. Drug-tolerant persister cancer cells are vulnerable to GPX4 inhibition. *Nature*. 2017;551:247.
24. Dependency of a therapy-resistant state of cancer cells on a lipid peroxidase pathway. *Nature*. 2017;547:453–7.
25. Meng X, Jian D, Liu F, Guo T, Zhao Y. Triggered All-Active Metal Organic Framework: ferroptosis machinery contributes to the apoptotic photodynamic antitumor therapy. *Nano Lett*. 2019;19:7866–76.
26. Zhu T, Shi L, Yu C, Dong Y, Qiu F, Shen L, et al. Ferroptosis promotes photodynamic therapy: supramolecular photosensitizer-inducer nanodrug for enhanced cancer treatment. *Theranostics*. 2019;18(11):3293–307. 9).
27. Zhang R, Zhang L, Ran H, Li P, Wang Z. Mitochondria-Targeted Anticancer Nanoplatfom with Deep Penetration for Enhanced Synergistic Sonodynamic and Starvation Therapy. *Biomater Sci*. 2020;21(16):4581–94. 8).
28. MAEDA H. Vascular permeability in cancer and infection as related to macromolecular drug delivery, with emphasis on the EPR effect for tumor-selective drug targeting. *Proc Jpn Acad Ser B Phys Biol Sci*. 2012;88:53–71.
29. Tang Y, Wang X, Li J, Nie Y, Li C. Overcoming the reticuloendothelial system barrier to drug delivery with a "Don't-Eat-Us" Strategy. *ACS Nano*. 2019;13(11):13015–26.
30. Qingzhi J, Chi, Zhang, Huilan W, et al. Mitochondria-targeting immunogenic cell death inducer improves the adoptive T-cell therapy against solid tumor. *Front Oncol*. 2019;12:9: 1196.
31. Jain RK, Stylianopoulos T. Delivering nanomedicine to solid tumors. *Nat Rev Clin Oncol*. 2010;7:653–64.
32. Zhang L, Yi H, Song J, Huang J, Yang K, Tan B, et al. Mitochondria-targeted and ultrasound-activated nanodroplets for enhanced deep-penetration sonodynamic cancer therapy. *ACS Appl Mater Interfaces*. 2019;6(9):9355–66. 11.
33. Wang X, Chen H, Zeng X, Guo W, Yu J, Shan W, et al. Efficient lung cancer-targeted drug delivery via a nanoparticle/MSC System. *Acta Pharm Sin B*. 2019;9(1):167–76.
34. Yu Y, Ibrahim N, Walsh WR, Yang JL. Abstract LB-295: Targeted therapy of human osteosarcoma cell lines. *Can Res*. 2012;72:LB–295.
35. Jw A, Jz A, Ntdn B, Yac C, Jth C, Xd A. Quantitative measurements of IR780 in formulations and tissues. *J Pharm Biomed Anal*. 2020;5:194:113780.
36. Zhu H, Chen X, Peng C, Pu K. Organic Nanotheranostics for photoacoustic imaging-guided phototherapy. *Curr Med Chem*. 2019;26(8):1389–405.

37. Fan J, Kamphorst JJ, Mathew R, Chung MK, White E, Shlomi T, et al. Glutamine-driven oxidative phosphorylation is a major ATP source in transformed mammalian cells in both normoxia and hypoxia. *Mol Syst Biol.* 2013; 3;9:712.
38. Xiang Q, Qiao B, Luo Y, Cao J, Wang Z. Increased photodynamic therapy sensitization in tumors using a nitric oxide-based nanoplatfrom with ATP-production blocking capability. *Theranostics.* 2021;11:1953–69.
39. Burke PJ, Mitochondria. Bioenergetics and Apoptosis in Cancer. *Trends Cancer.* 2017;3:857–70.
40. Wang H, Liu C, Zhao Y, Gao G. Mitochondria regulation in ferroptosis. *Eur J Cell Biol.* 2019;99:151058.
41. Wan SY, Kim KJ, Gaschler MM, Patel M, Stockwell BR. Peroxidation of polyunsaturated fatty acids by lipoxygenases drives ferroptosis. *Proc Natl Acad Sci U S A.* 2016;113:E4966.
42. Ma D, Li C, Jiang P, Jiang Y, Zhang D. Inhibition of ferroptosis attenuates acute kidney injury in rats with severe acute pancreatitis. *Dig Dis Sci.* 2020;66(2):483–92.
43. Yuan H, Han Z, Chen Y, Qi F, Fang H, Guo Z, Zhang S, et al. Ferroptosis photoinduced by new cyclometalated iridium(III) complexes and its synergism with apoptosis in tumor cell inhibition. *Angew Chem Int Ed Engl.* 2021;6(15):8174–81. 60).
44. Dixon SJ, Lemberg KM, Lamprecht MR, et al. Ferroptosis: An iron-dependent form of nonapoptotic cell death. *Cell.* 2012;25(5):1060–72. 149.
45. Ma L, Zhang X, Yu K, Xu X, Wang J. Targeting SLC3A2 subunit of system XC- is essential for m6A Reader YTHDC2 to be an endogenous ferroptosis inducer in lung adenocarcinoma. *Free Radic Biol Med.* 2021;168:25–43.
46. Xiaoxu W, Steven P, Gygi J, et al. Quantitative proteomics identifies NCOA4 as the cargo receptor mediating ferritinophagy. *Nature.* 2014;1(7498):105–9. 509.
47. Roberto B, Giorgia F, Matte' A, et al. NCOA4 deficiency impairs systemic iron homeostasis. *Cell Rep.* 2016;26(3):411–21. 14).
48. Naiara S-C, Joseph M. The Role of NCOA4-mediated ferritinophagy in health and disease. *Pharmaceuticals (Basel).* 2018; 23;11(4):114.
49. Wang Y, Deng X, Yu C, Zhao G, Zhou J, Zhang G, et al. Synergistic inhibitory effects of capsaicin combined with cisplatin on human osteosarcoma in culture and in xenografts. *J Exp Clin Cancer Res.* 2018;16(1):251. 37.
50. Sidoroff A, Thaler P. Taking treatment decisions in non-melanoma skin cancer—the place for topical photodynamic therapy (PDT). *Photodiagnosis Photodyn Ther.* 2010;7:24–32.
51. Dd A, Js B, Dpa C, Ara D, Hua CA, Nu A, et al. PEG-PLGA nanospheres loaded with nanoscintillators and photosensitizers for radiation-activated photodynamic therapy. *Acta Biomater.* 2020;117:335–48.
52. Silva M, Videira PA, Sackstein R. E-Selectin ligands in the human mononuclear phagocyte system: implications for infection, inflammation, and immunotherapy. *Front Immunol.* 2017;8:1878.

53. Fernandes I, Melo-Alvim C, Lopes-Brás R, Esperana-Martins M, Costa L. Osteosarcoma pathogenesis leads the way to new target treatments. *Int J Mol Sci.* 22: 813.
54. Hycab C, Jiang D, Yu W, Cqwab C, Xian L, Hwdab C. Hybrid cell membrane-coated nanoparticles: A multifunctional biomimetic platform for cancer diagnosis and therapy *ScienceDirect. Acta Biomater.* 2020;112:1–13.
55. Can W, Yulan L, Zhang R, et al. Pretreated macrophage-membrane-coated gold nanocages for precise drug delivery for treatment of bacterial infections. *Adv Mater.* 2018;30(46):e1804023.
56. Xia Q, Zhang Y, Li Z, Hou X, Feng N. Red blood cell membrane-camouflaged nanoparticles: A novel drug delivery system for antitumor application. *Acta Pharm Sin B.* 2019;9(4):675–89.
57. Rao L, Bu LL, Cai B, Xu JH, Li A, Zhang WF, Sun ZJ, Guo SS, Liu W, Wang TH, Zhao XZ. Cancer cell membrane-coated upconversion nanoprobe for highly specific tumor imaging. *Adv Mater.* 2016;28(18):3460–6.
58. Fang D, Maldonado EN. VDAC Regulation: A mitochondrial target to stop cell proliferation. *Adv Cancer Res.* 2018;138:41–69.
59. Pan GY, Jia HR, Zhu YX, Wang RH, Wu FG, Chen Z. Dual channel activatable cyanine dye for mitochondrial imaging and mitochondria-targeted cancer theranostics. *ACS Biomater Sci Eng.* 2017;11(3 (12)):3596–606.
60. Wallace DC. Mitochondria and cancer. *Nat Rev Cancer.* 2012;12:685.
61. Chao Z, Tao L, Su Y, Luo S, Zhu Y, Tan X, et al. A near-infrared fluorescent heptamethine indocyanine dye with preferential tumor accumulation for in vivo imaging. *Biomaterials.* 2010;31:6612–7.
62. Erlong Z, Shenglin, Luo, Xu T, et al. Mechanistic study of IR-780 dye as a potential tumor targeting and drug delivery agent - *ScienceDirect. Biomaterials.* 2014;35:771–8.
63. Basu A. Crosstalk between extrinsic and intrinsic cell death pathways in pancreatic cancer: synergistic action of estrogen metabolite and ligands of death receptor family. *Cancer Res.* 2006;66:4309–18.
64. Lian-Jiu J-H, Zhang, Hernando, Gomez R, et al. Reactive oxygen species-induced lipid peroxidation in apoptosis, autophagy, and ferroptosis. *Oxid Med Cell Longev.* 2019; 2019: 5080843.
65. Bennett BD, Gralnick JA. Mechanisms of toxicity by and resistance to ferrous iron in anaerobic systems. *Free Radic Biol Med.* 2019;20:140:167–71.
66. Xu X, Chen Y, Zhang Y, Yao Y, Ji P. Highly stable and biocompatible hyaluronic acid-rehabilitated nanoscale MOF-Fe₂ + induced ferroptosis in breast cancer cells. *J Mater Chem B.* 2020;18:9129–38.

Figures

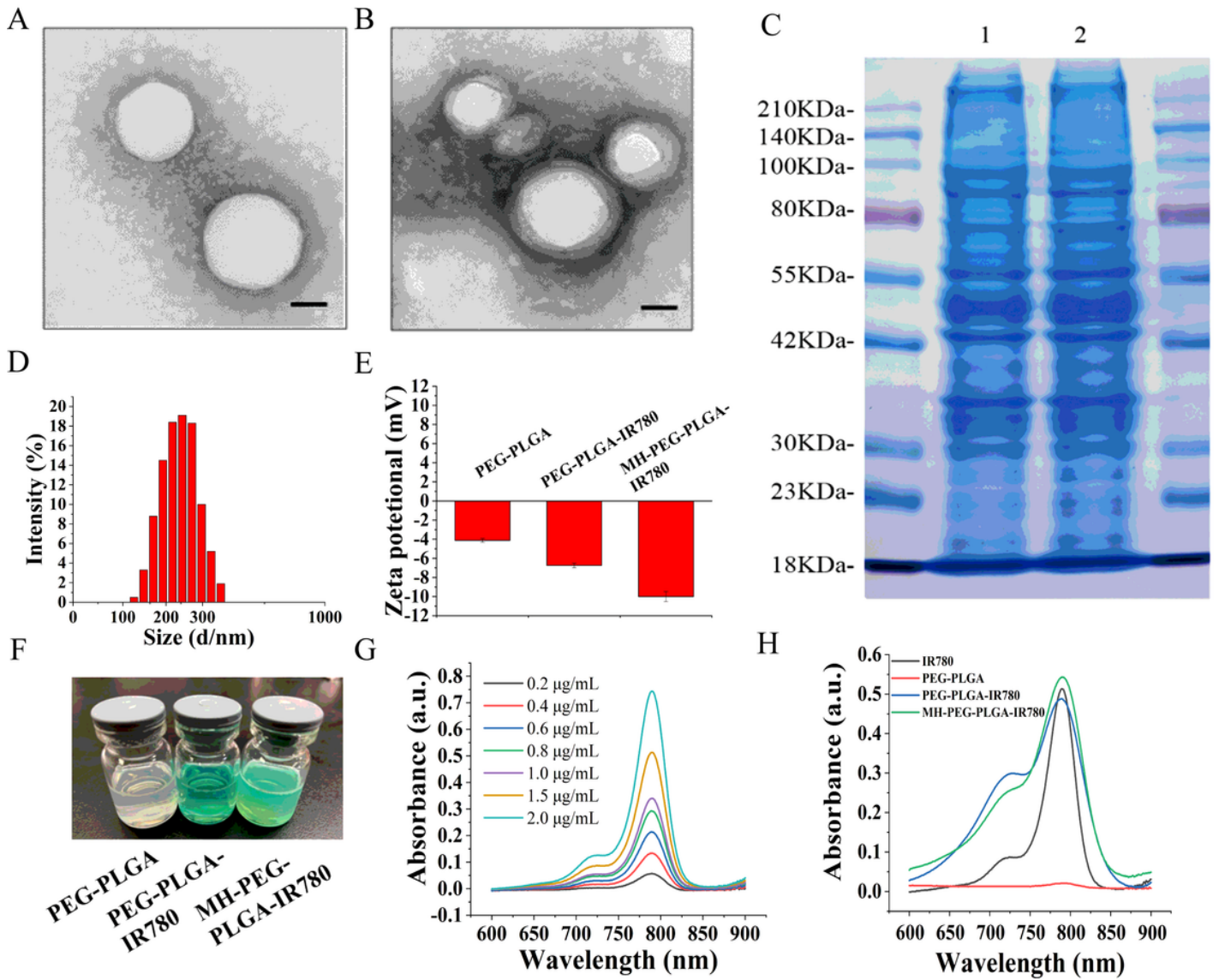


Figure 1

Characterizations of the MH-PEG-PLGA-IR780 NPs. A-B) TEM images of PEG-PLGA NPs and MH-PEG-PLGA NPs. (scale bar: 100 nm). C) SDS-PAGE protein analysis results. 1: MH, 2: MH-PEG-PLGA NPs. D) Size distribution of the MH-PEG-PLGA-IR780 NPs was measured by DLS. E-F) Zeta potential (n = 3) and digital photos of different NPs (PEG-PLGA NPs, PEG-PLGA-IR780 NPs, and MH-PEG-PLGA-IR780 NPs). G) UV-vis spectra of single IR780, PEG-PLGA NPs, PEG-PLGA-IR780 NPs, and MH-PEG-PLGA-IR780 NPs. H) Absorbance spectra of IR780 in a concentration-dependent manner as recorded by UV-vis spectrum.

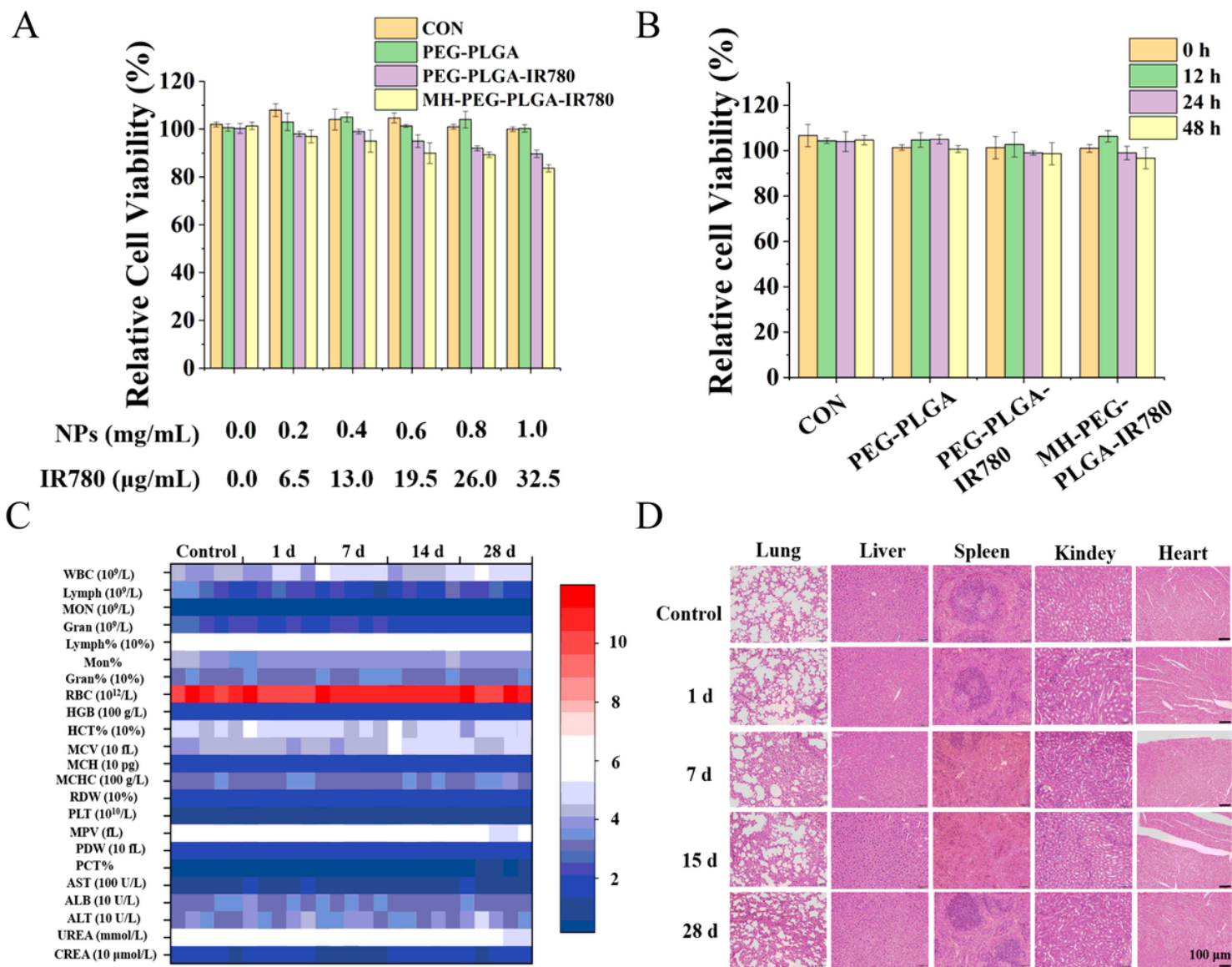


Figure 2

Biosafety of the MH-PEG-PLGA-IR780 NPs. A) Relative viability (%) of HOS cells after coincubation with a wide range of NPs concentrations. B) Relative viability (%) of HOS cells after coincubation with MH-PEG-PLGA-IR780 NPs (PEG-PLGA: 0.4 mg/mL) at prolonged time points. (The data are presented as the mean \pm SD). C-D) Blood index (routine blood and biochemistry) and H&E staining of the main organs (heart, liver, spleen, lung and kidney) of BALB/c nude mice were collected at 0, 1, 7, 14, 28 days after post-injection of MH-PEG-PLGA-IR780 NPs. (n = 5). The scale bars are 100 μ m.

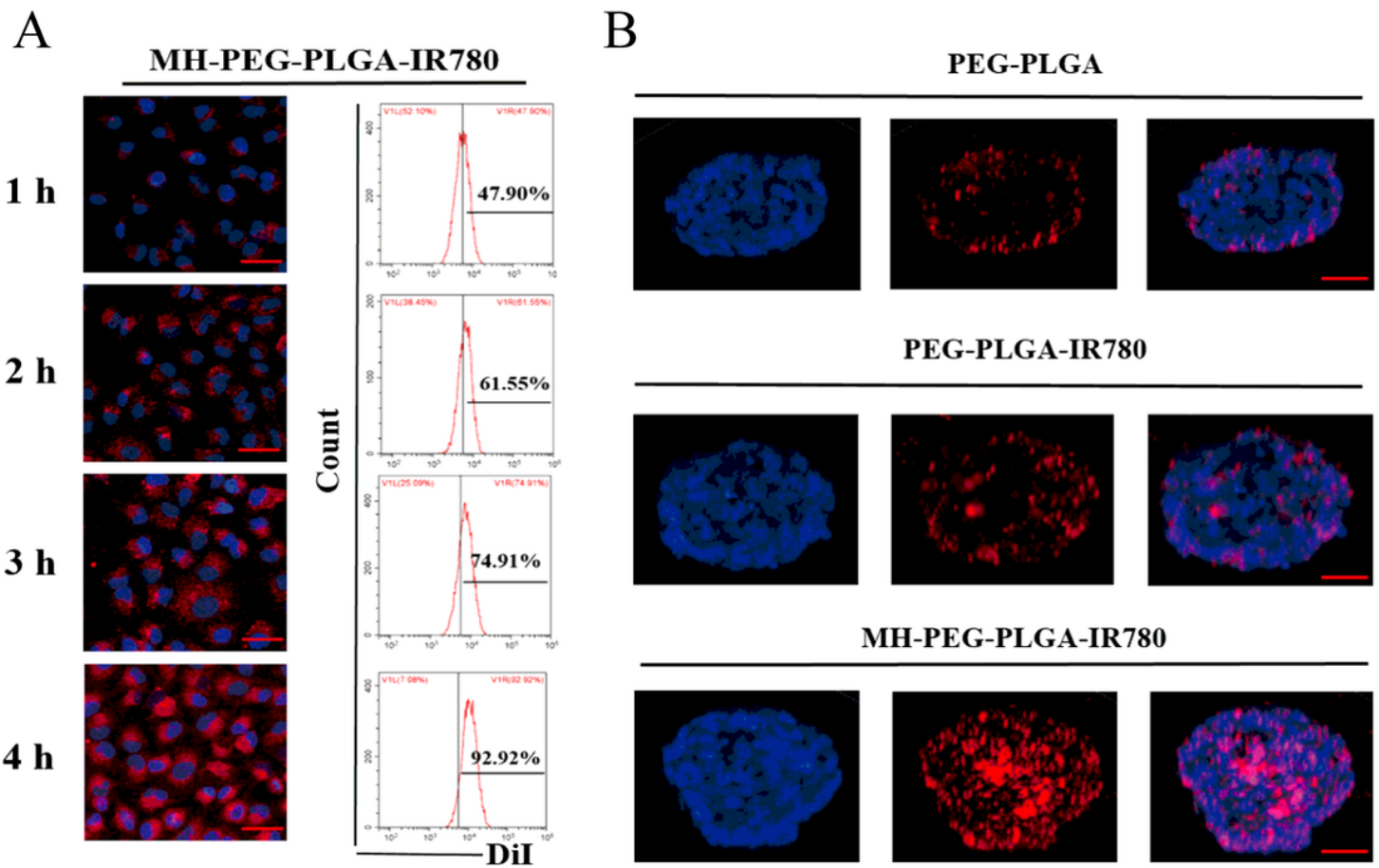


Figure 3

A) Intracellular uptake of MH-PEG-PLGA-IR780 NPs (labeled with DiI) as measured by CLSM and FC analysis at prolonged coincubation times. The scale bars are 50 μm . B) The penetration capability of PEG-PLGA NPs, PEG-PLGA-IR780 NPs, and MH-PEG-PLGA-IR780 NPs in 3D tumor spheroids were observed by CLSM. The scale bars are 50 μm .

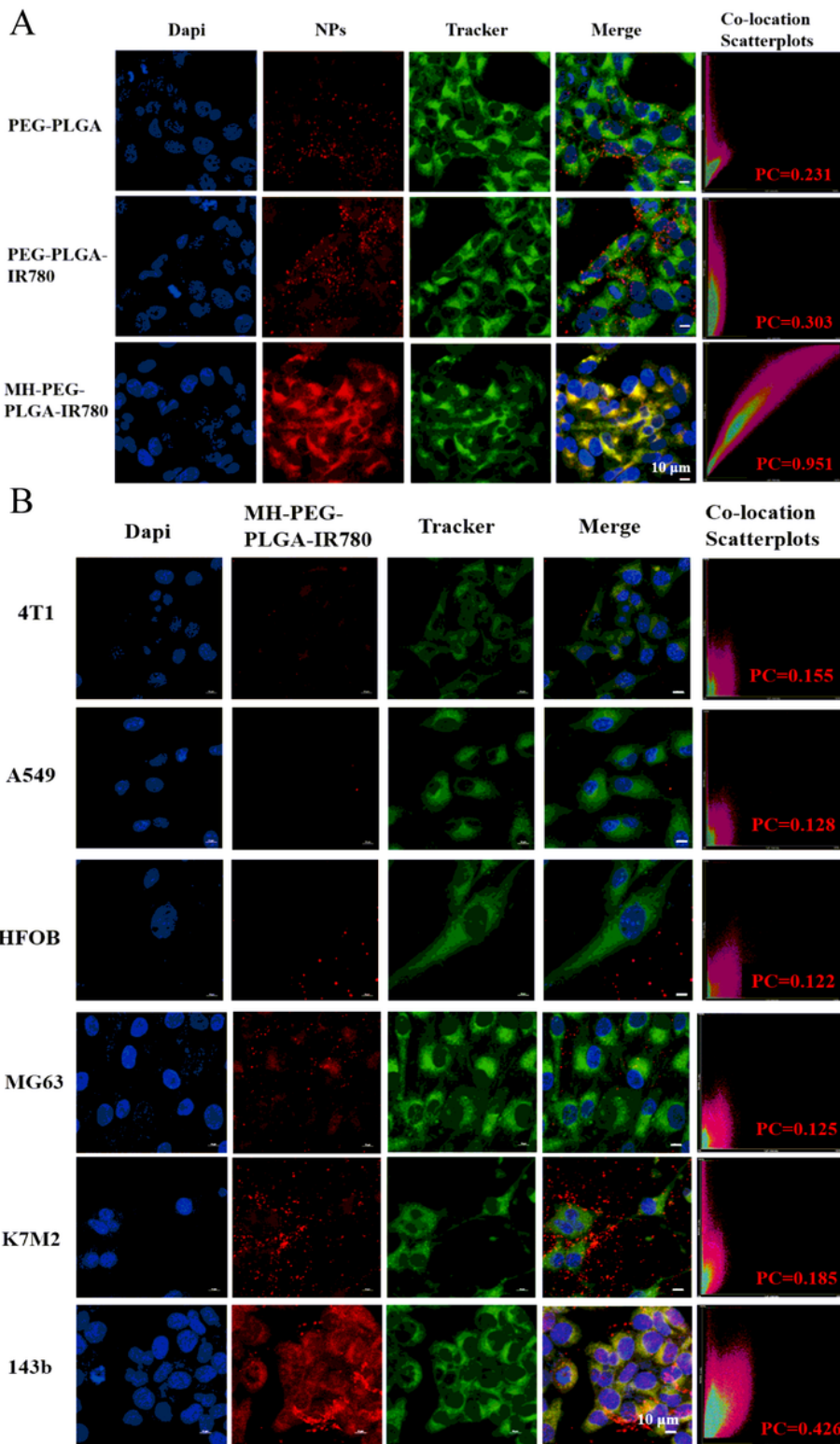


Figure 4

A) Mitochondrial location of the NPs (PEG-PLGA NPs, PEG-PLGA-IR780 NPs, MH-PEG-PLGA-IR780 NPs) in HOS cells were observed by CLSM. The scale bars are 10 μ m. B) MH-PEG-PLGA-IR780 NPs colocalized with mitochondria (stained with MitoTracker) in different kinds of cells (4T1, A549, HFOB 1.19, MG63, K7M2 and 143B) as illustrated by CLSM. The scale bars are 10 μ m.

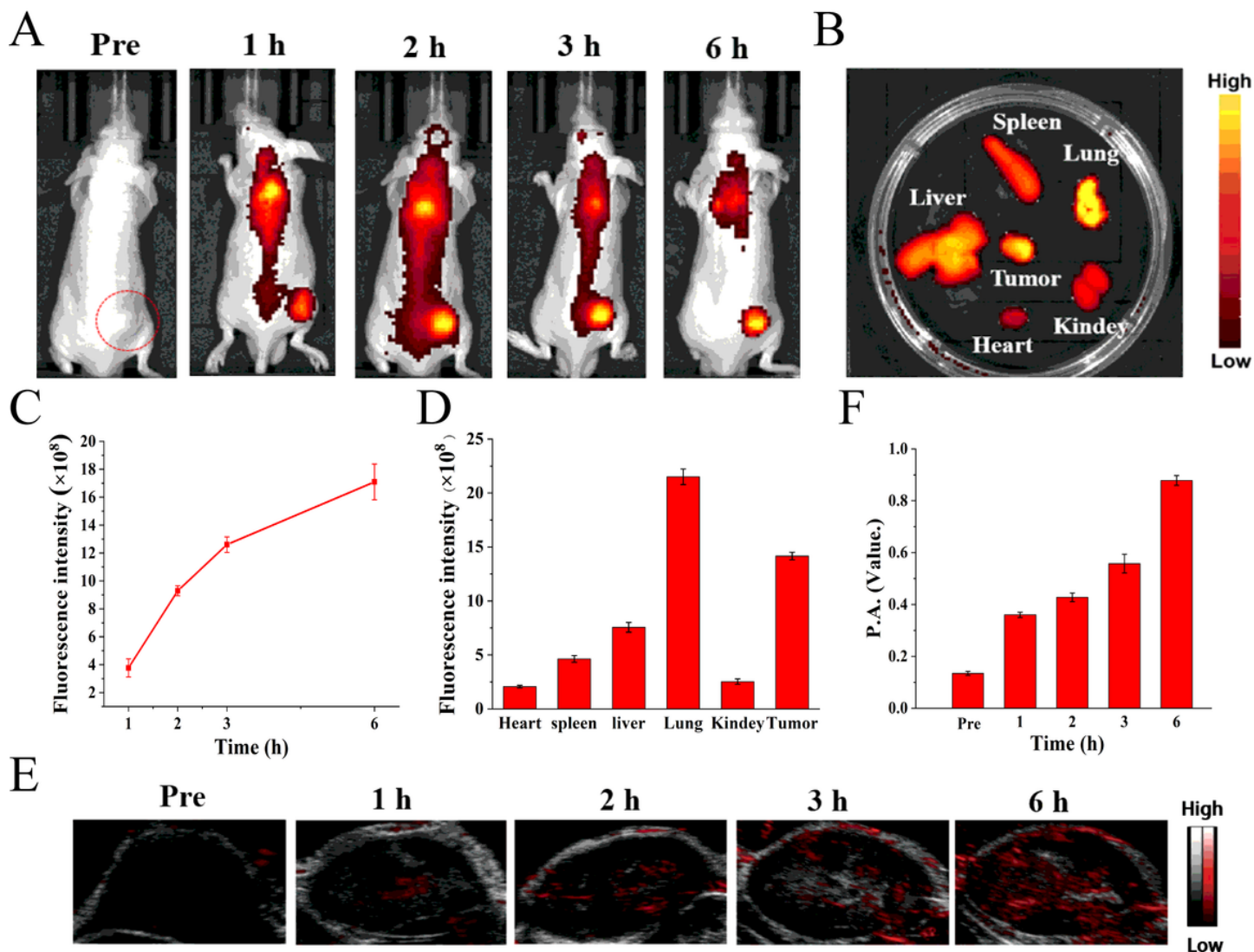
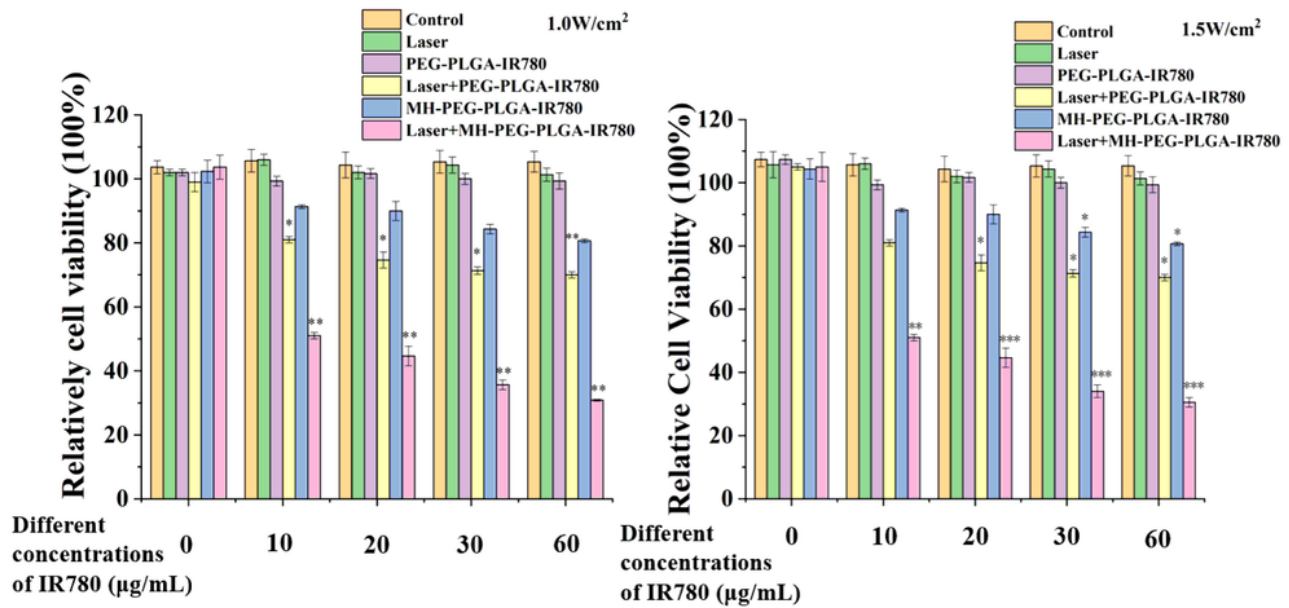


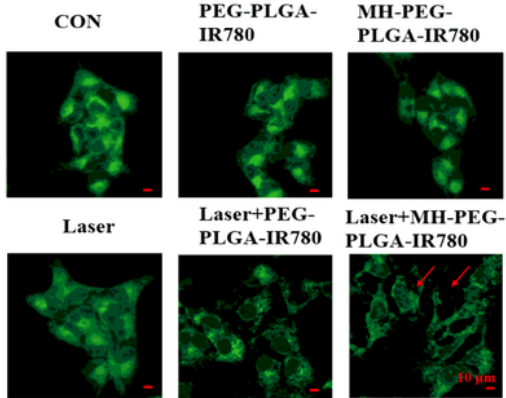
Figure 5

FL/PA imaging of the MH-PEG-PLGA-IR780 NPs in vivo. A, C) FL images of HOS tumor-bearing mice and quantitative FL signal intensities within tumor regions after intravenous injection of MH-PEG-PLGA-IR780 NPs at prolonged time points. B) Ex vivo FL imaging of the tumor and major organs harvested from mice after 6 h post-injection. D) Quantitative biodistribution of tumors and major organs ex vivo were measured by the average FL intensities. E-F) PA images and quantitative PA signal intensities of tumor regions after intravenous administration at corresponding time points. (The data are presented as the mean \pm SD, n = 3).

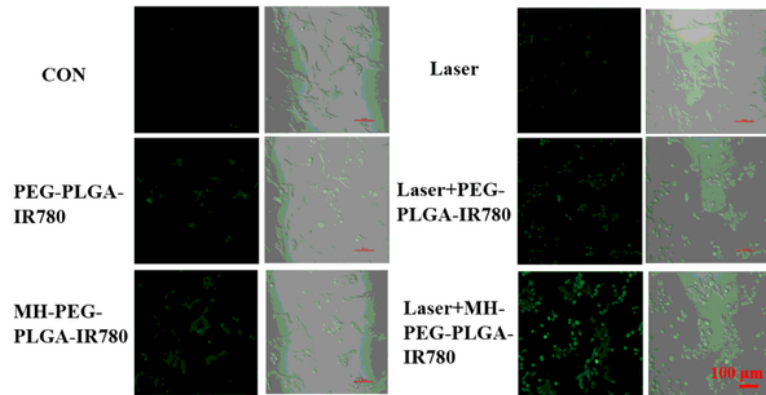
A



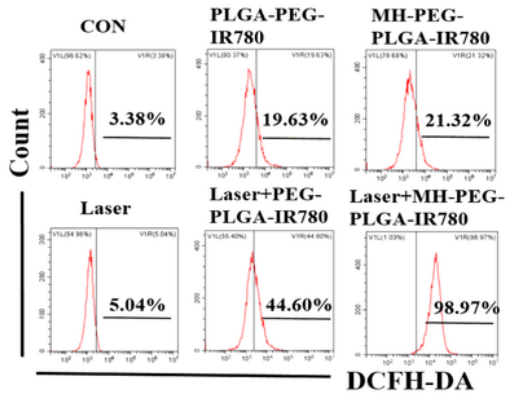
B



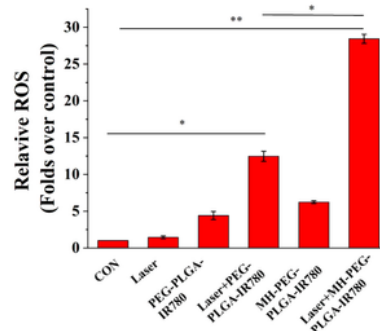
C



D



E



F

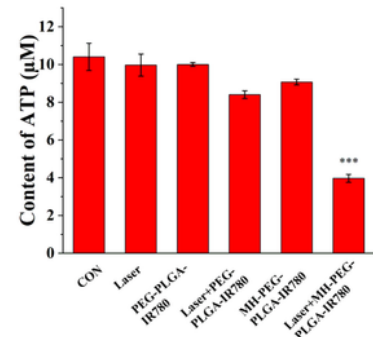


Figure 6

PDT performance with the assist of homologous and mitochondrial targeting. A) Relative cell viability (%) of HOS by various treatments. B) Aggravated mitochondrial fragmentation of HOS cells after targeted PDT treatment. The scale bars are 10 µm. C-E) CLSM images and FC analysis of the production of ROS levels in HOS cells (stained with DCFH-DA) after different managements. The scale bars are 100 µm. (The

data are presented as the mean \pm SD, $n = 3$, $*p < 0.05$, $**p < 0.01$). F) The content of ATP in HOS cells after different treatments (The data are presented as the mean \pm SD, $n = 3$, $***p < 0.001$).

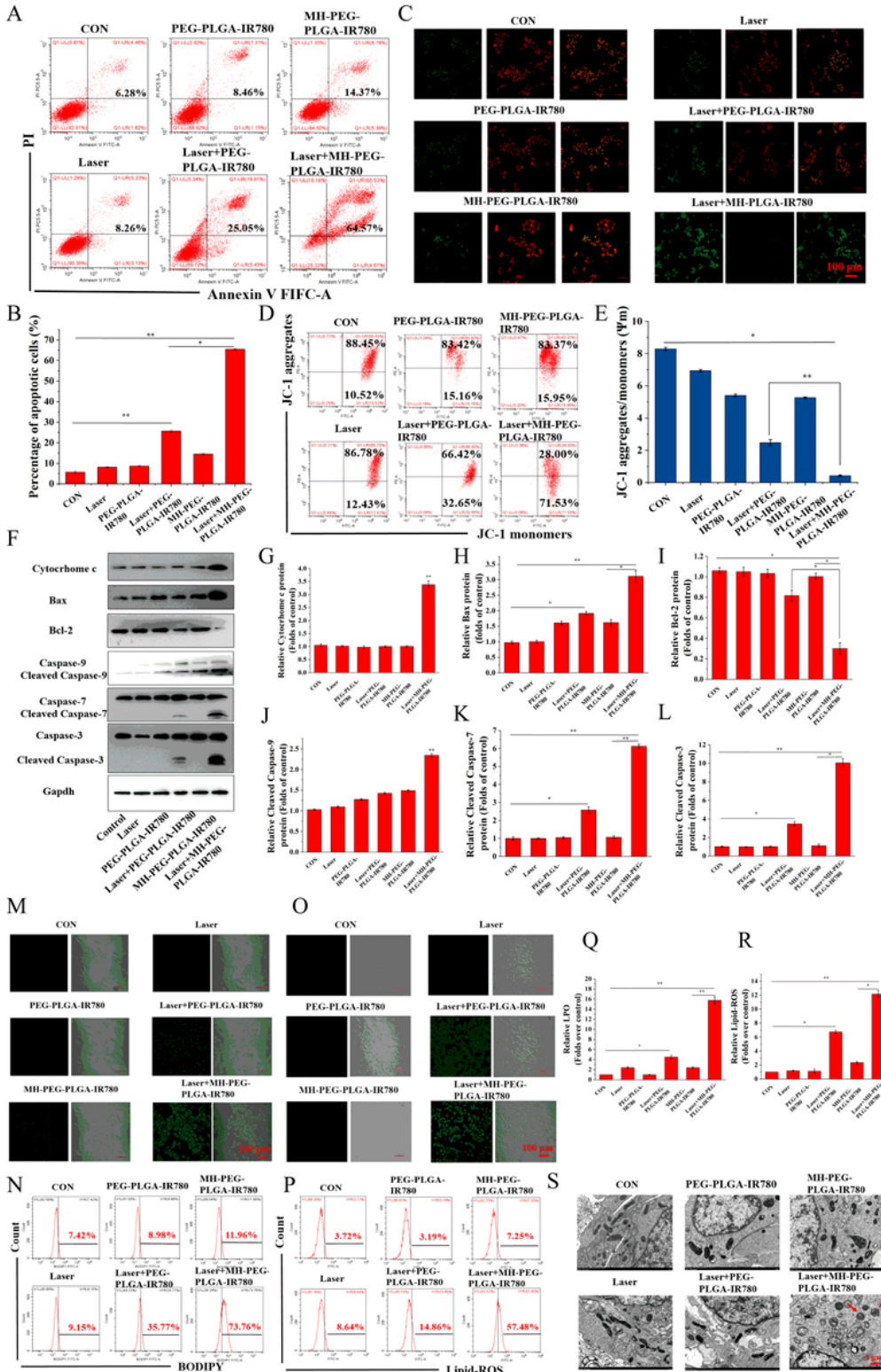


Figure 7

Evaluation of apoptosis and ferroptosis. A-B) Induction of apoptosis in HOS cells (stained with annexin V-FITC/PI) after various treatments by FC analysis. (The data are presented as the mean \pm SD, $n = 3$, $*p < 0.05$, $**p < 0.01$). C-E) The changes of $\Delta\psi_m$ in HOS cells stained with JC-1 after various managements as

observed via CLSM and FC. The scale bars are 100 μm . F) The expression levels of cell apoptosis-related proteins were measured by western blot. G-L) Statistical analyses of cytochrome C, Bax, Bcl-2, cleaved caspase-9, cleaved caspase-7 and cleaved caspase-3. (The data are presented as the mean \pm SD, $n = 3$, * $p < 0.05$, ** $p < 0.01$). M-R) The excessive production of LPO and Lipid-ROS in HOS cells after targeted PDT treatment as measured by CLSM and FC. (The data are presented as the mean \pm SD, $n = 3$, * $p < 0.05$, ** $p < 0.01$). The scale bars are 100 μm . S) The morphology of mitochondria after various treatments as observed by TEM. The scale bars are 1 μm .

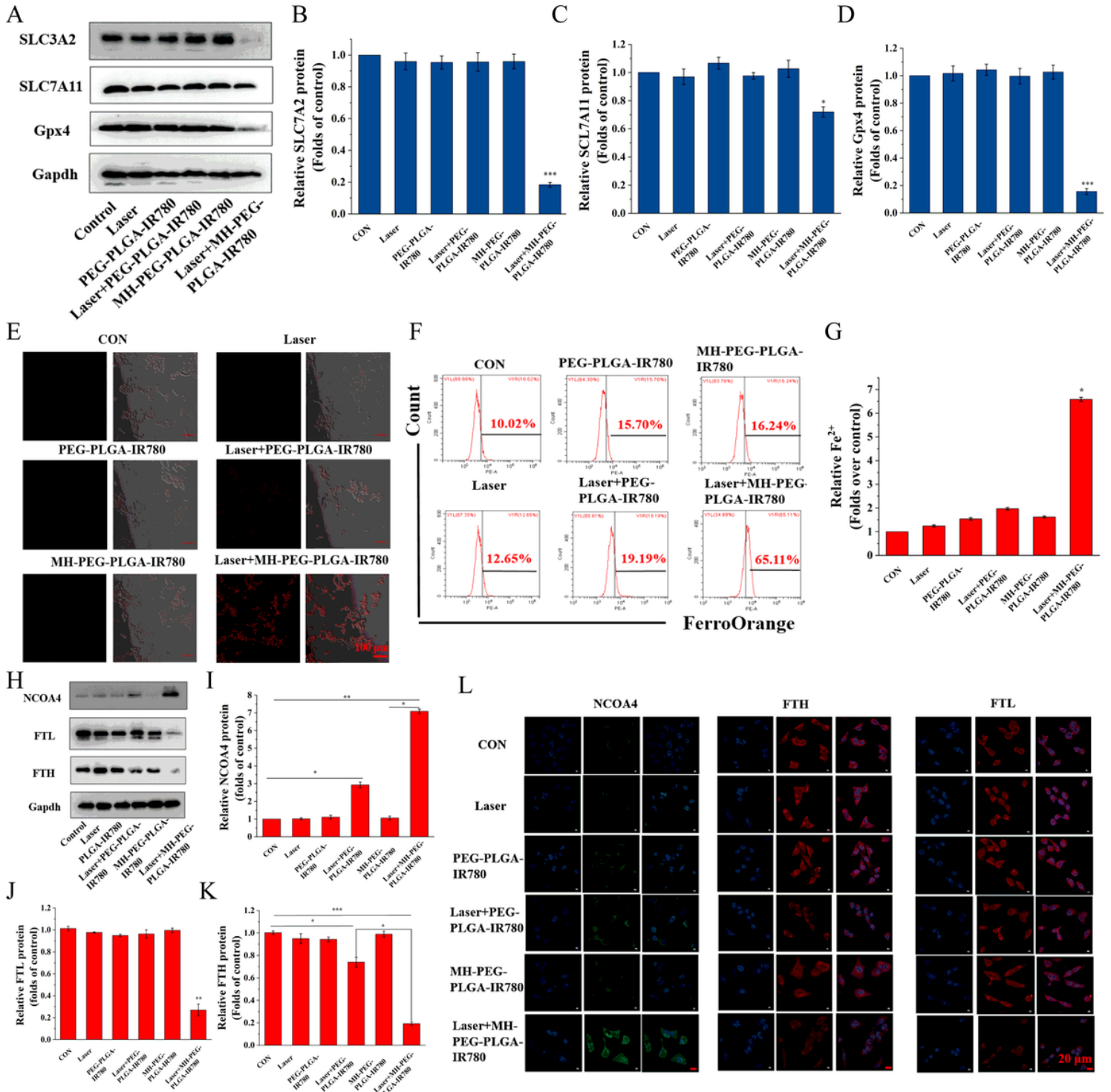


Figure 8

The specific mechanism of the induction of ferroptosis by targeted PDT treatment. A) The expression levels of ferroptosis-related proteins after different managements detected by western blot. B-D) Statistical analyses of SLC7A11 and SLC3A2. (The data are presented as the mean \pm SD, $n = 3$, $*p < 0.05$, $***p < 0.001$). E-G) Enhanced intracellular Fe²⁺ production of targeted PDT treatment in HOS cells. CLSM images (labeled with FerroOrange) and FC analysis of Fe²⁺ generation after different treatments. (The data are presented as the mean \pm SD, $n = 3$, $*p < 0.05$). The scale bars are 100 μ m. H) Western blot analyses of the expression levels of ferritinophagy-related proteins after various treatments. I-K) Statistical analyses of NCOA4, FTH and FTL. (The data are presented as the mean \pm SD, $n = 3$, $*p < 0.05$, $**p < 0.01$, $***p < 0.001$). L) IF images of NCOA4, FTH and FTL in HOS cells after different managements. The scale bars are 20 μ m.

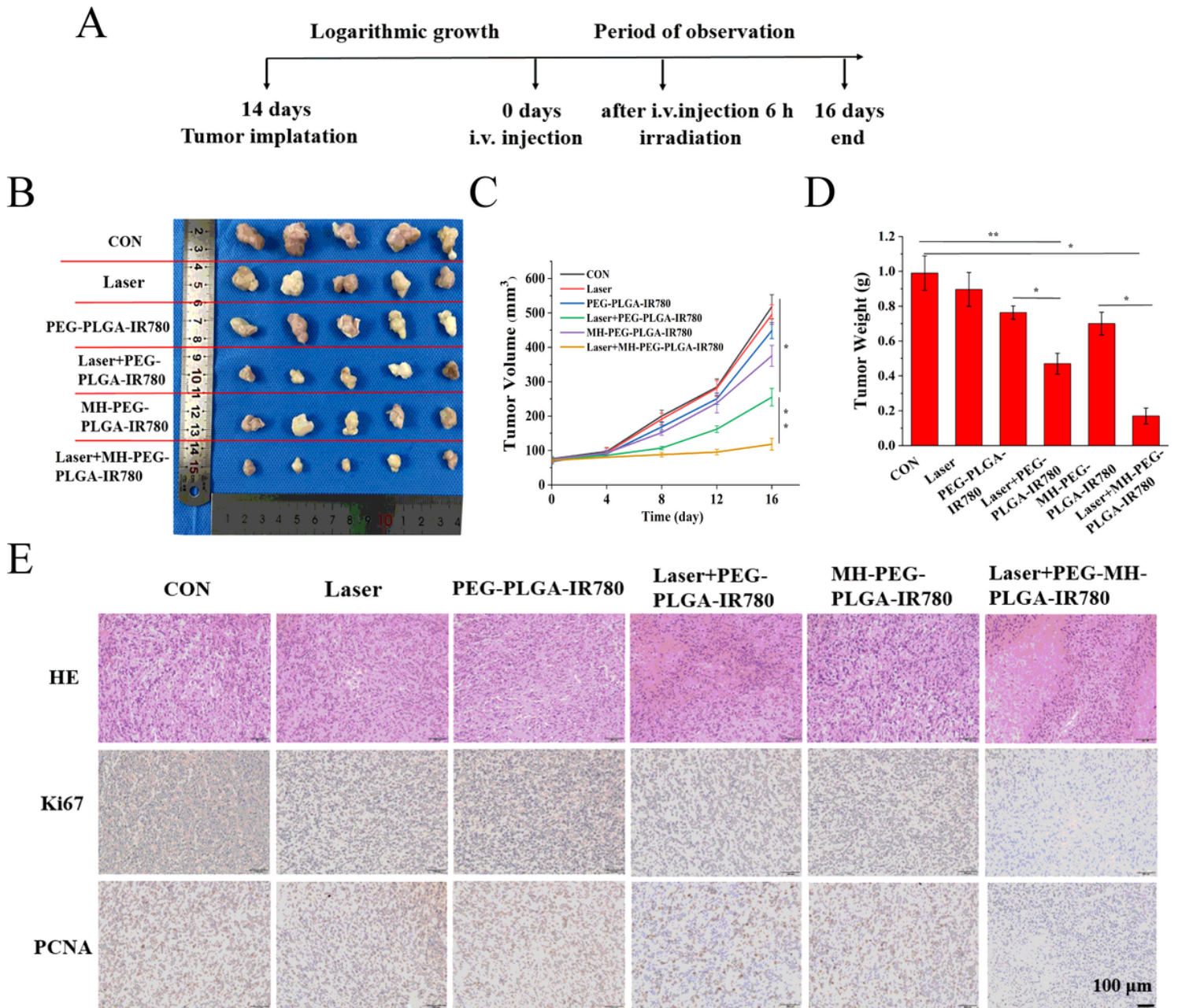


Figure 9

Antitumor capacity in vivo. A) Schedule of the targeted PDT treatment. B) Photographs of tumors harvested from mice after various treatments (n = 5) and HOS tumor-bearing mice before sacrifice. C) Tumor volume was measured during therapeutic period. (The data are presented as the mean \pm SD, n = 5, *p < 0.05, **p < 0.01). D) Tumor weights were recorded at the end of therapy. (The data are presented as the mean \pm SD, n = 5, *p < 0.05, **p < 0.01). E) H&E staining, IHC images of PCNA and Ki67 on tumor specimens after various treatments. The scale bars are 100 μ m.

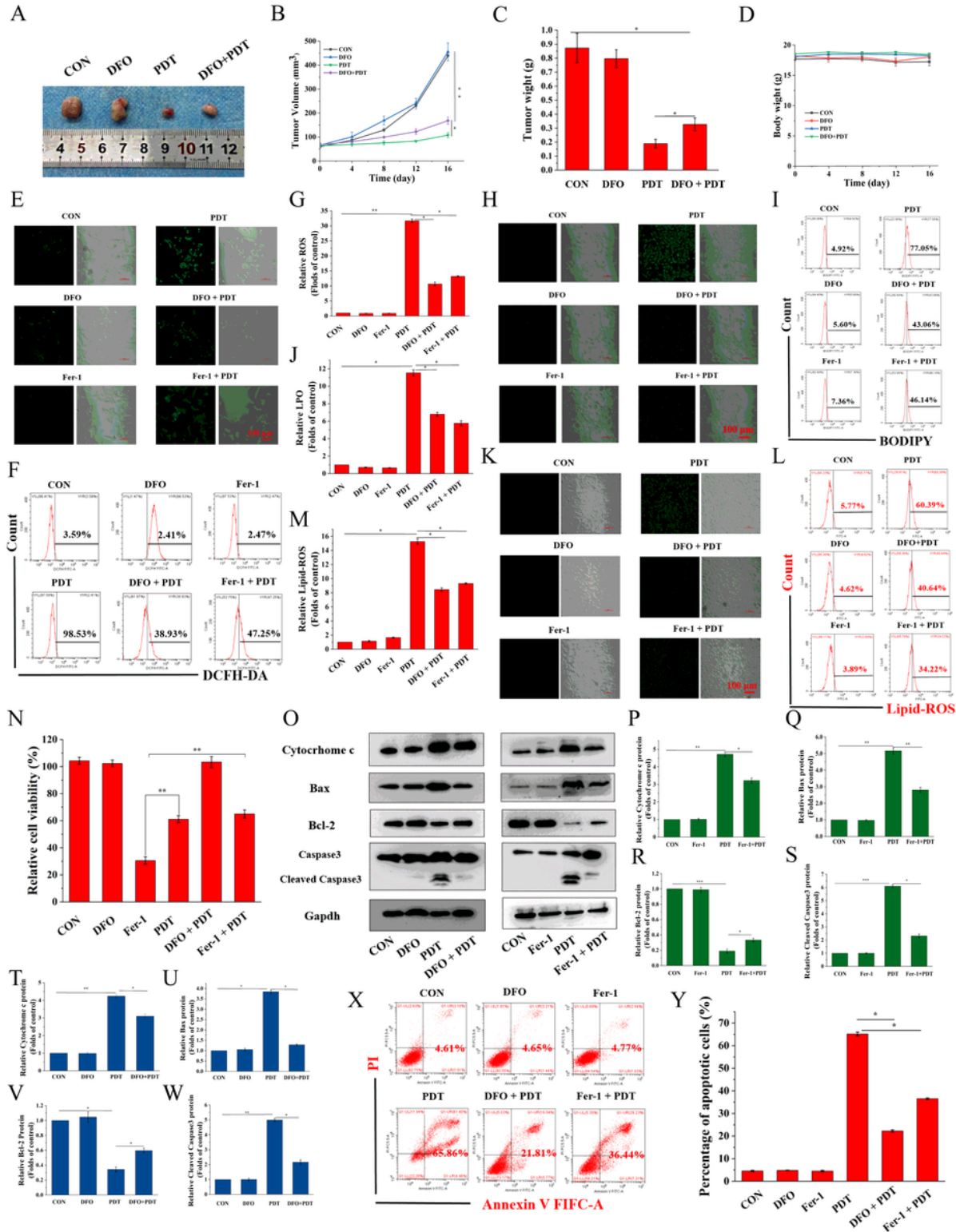


Figure 10

A) Representative images of tumors collected from mice after various therapies. B-D) Tumor volume, tumor weight and the weight of mice were measured during therapeutic period. (The data are presented as the mean \pm SD, n = 5, *p < 0.05, **p < 0.01). E-L) CLSM and FC analyses of the intracellular ROS, LPO and Lipid-ROS levels by PDT after pretreatments of DFO and Fer-1. (The data are presented as the mean \pm SD, n = 3, *p < 0.05, **p < 0.01). The scale bars are 100 μ m. N) The decreased relative cell viability (%) of HOS cells of PDT via the preincubation of DFO and Fer-1. (The data are presented as the mean \pm SD, n = 3, **p < 0.01). O) After ferroptosis scavenging by DFO and Fer-1, the expression levels of cell apoptosis-related proteins induced by PDT were measured by western blot. P-W) Statistical analyses of cytochrome C, Bax, Bcl-2, cleaved caspase-3 by pretreatment of DFO and Fer-1 followed PDT. (The data are presented as the mean \pm SD, n = 3, *p < 0.05, **p < 0.01, ***p < 0.001) X-Y) The suppression of cell apoptosis percentages (stained with annexin V-FITC/PI) by the inhibition of ferroptosis as determined by FC. The data are presented as the mean \pm SD, n = 3, *p < 0.05). PDT: laser+MH-PEG-PLGA-IR780 NPs.

Supplementary Files

This is a list of supplementary files associated with this preprint. Click to download.

- [SupportingInformationJECCR.docx](#)
- [floatimage1.jpeg](#)